Pd model catalysts: Effect of air pulse length during redox aging on Pd redispersion

Jason A. Lupescu [a,b,*], Johannes W. Schwank [a], Galen B. Fisher [a], Jon Hangas [b], Sabrina L. Peczonczyk [b], William A. Paxton [b]

[a] University of Michigan, Ann Arbor, MI 48109, USA
[b] Ford Motor Company, Dearborn, MI 48124, USA

ARTICLE INFO

ABSTRACT

Nano-sized noble metal particles are an essential component in automotive catalytic converters. However, during customer in-use operation they agglomerate into larger particles and the performance of the catalytic converter is negatively affected. Engine control methods are needed to provide an environment capable of redispersing noble metal catalyst particles while the particle size is still small. In this study, Pd model powder catalysts, supported on three-way catalytic converter washcoat components of ceria-zirconia (Pd/CZO), 4 wt% La_2O_3 stabilized γ-Al_2O_3 (Pd/Al) and unstabilized γ-Al_2O_3 (Pd/A) were exposed to redox cycling at 700 °C for 16 h (to simulate customer in-use operation engine exhaust) either continuously or interrupted with brief air pulses. The two goals of this research were to determine the air pulse length required so that any Pd redispersion gains achieved by air treatment in each 20 min redox cycle will be retained by the end of the 16 h aging, and to determine if these supports enable rapid Pd redispersion on the time scale of a common ~10 s engine fuel cut. Pd particle size and dispersion measurements were performed with three complimentary techniques of H_2 chemisorption, XRD and electron microscopy since not one technique could be used exclusively. Catalyst activity was determined by CO oxidation with the Water Gas Shift (WGS) reaction and Oxygen Storage Capacity (OSC) measurements to probe the contact between the noble metal and support at a given state of catalyst deterioration, and a CO light-off test to confirm trends observed with Pd metal dispersion. We found that air pulses lasting for 1/6 min applied to interrupt short redox aging spans enabled Pd redispersion only on the Pd/Al catalysts. Strong metal support interaction on the Pd/CZO catalysts by decoration of the Pd surface with support oxide was suspected to slow Pd redispersion by limiting metal mobility. Support oxides that promote the Pd^{2+} state may have been required on the Pd catalysts in order to exhibit Pd redispersion. The insight gained from this work could be used to develop engine control and aftertreatment systems that actively intervene and regenerate a catalyst capable of rapid Pd redispersion.

© 2017 Elsevier B.V. All rights reserved.

1. Introduction

Automotive catalytic converters are irreversibly deactivated by exposure to combustion exhaust under in-use operating temperatures (500 °C–900 °C) and by more severe rapid aging protocols (>1000 °C) used to simulate 150,000 miles of in-use operation in just hours. The catalytic converter or Three-Way Catalyst (TWC) washcoat technology contains noble metals (Pt, Pd and/or Rh) impregnated onto a complex support material that includes alu-

mina to provide high surface area, lanthana (La_2O_3) to stabilize the alumina surface area against steam and mixed oxides of ceria and zirconia (CZO) for oxygen storage capacity (OSC) promotion [1–3]. Precious metals are known to undergo sintering causing loss of catalytic activity.

Previous attempts to counteract the sintering induced loss of Pd dispersion relied upon feeding excess oxygen to deactivated TWC samples aged under in-use operating temperatures [4–7] or under more mild conditions [8,9]. These works achieved modest gains in Pd dispersion and partial regeneration of activity. The fundamentals behind this Pd redispersion were revealed in earlier electron microscopy work during heating of Pd/Al_2O_3 thin film catalysts in oxygen and observing that Pd changed to PdO above 325 °C then wet and spread over the support between 350 °C and 800 °C,

and finally mobile PdO particles ruptured over the support surface and redispersed [10–12]. While PdO is the prerequisite for redispersion [6], support collapse and metal-support interaction may limit PdO mobility and particle rupture. Other deactivation modes linked to strong metal support interaction (SMSI) include geometric effects where reducible oxide species partially block the active metal surface and weaken the interaction of adsorbates onto the Pd metal surface [13–18] and electronic effects where a negative binding energy shift indicates increased Pd electronegativity [19,20]. In our initial study with 700 °C redox aged Pd based model catalysts, a post-aging treatment in dry air at 700 °C for 2 h on the 1.5 wt% Pd supported on 4 wt% La$_2$O$_3$ stabilized γ-Al$_2$O$_3$ (Pd/Al) demonstrated: 1) reversal of SMSI effects, and 2) reduced Pd particle sizes [21]. However, the 1.5 wt% Pd supported on CeO$_2$-ZrO$_2$ mixed oxide (Pd/CZO) achieved just the first effect as decoration on Pd seemed to prevent Pd redispersion until the reduced support oxide species was removed from the Pd surface [21]. Our follow up study demonstrated that a two hour oxidizing gas treatment was more effective for Pd redispersion when performed when Pd particles were still relatively small rather than when the Pd particles were larger (8.8–13 nm) and more difficult to fully oxidize [22]. Small metal particles are thermodynamically less stable than larger particles since atoms on the particle surface are energetically less stable than the interior atoms already well ordered and packed. While it would be beneficial to conduct an in-situ regeneration of a catalytic converter, a two hour dry air treatment at 700 °C is not a realistic automotive operating exhaust condition. However, an operating condition of spaced short intervals of air at 700 °C would be analogous to common engine fuel cuts during a slowing down from high speed and each would last about 2–10 s [21]. Newton et al. showed that 2–10 s is enough time to redisperse very small (~3 nm) Pd particles on a fresh CZO-Al$_2$O$_3$ support during CO/NO cycling at 400 °C [8]. However, it is unclear if air exposure for such a short time is also sufficient to first counteract aging induced SMSI effects and then redisperse sintered Pd.

The goal of this investigation was to determine the length of interrupting air treatments during simulated automotive operating conditions that can limit or counteract Pd-based TWC deactivation on Al$_2$O$_3$ (Pd/A), 4wt%La$_2$O$_3$-Al$_2$O$_3$ (Pd/Al) and CZO (Pd/CZO) supports. Pd particle size and dispersion measurements were performed with three complimentary techniques of H$_2$ chemisorption, XRD and electron microscopy since not one technique could be used exclusively. H$_2$ chemisorption is vulnerable to errors from SMSI effects, XRD is insensitive to very small Pd particles (<6 nm) and electron microscopy has difficulty distinguishing Pd from CZO [4]. Carbon Monoxide (CO) adsorption infrared spectra were collected on the Pd catalyst samples to determine the surface characteristics based on the types of carbonaceous species formed and to identify the accessible Pd facets as performed in other works [13,23,24]. The oxygen storage capacity (OSC), CO light-off and water-gas shift (WGS) tests were included since the oxidation of CO gives insight into activity of the exposed Pd particle surface and contact between the Pd particle and support at a given state of catalyst deterioration.

2. Experimental

2.1. Preparation of model TWC samples

Pd-based powder catalysts of 1.5 wt% Pd supported on La$_2$O$_3$-doped γ-Al$_2$O$_3$ (Pd/Al) or ceria-zirconia (Pd/CZO), were prepared at a commercial catalyst washcoat supplier laboratory by incipient-wetness impregnation of these representative automotive TWC supports with a palladium solution free from chlorides. After drying, these catalysts were calcined at 500 °C for 4 h in air to fix the metals on the support materials. Previously, these Pd model
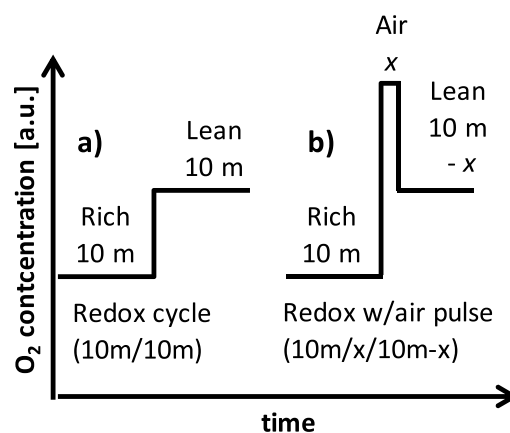

Fig. 1. Redox aging cycle and air pulse length.

catalysts were characterized to disclose the CZO as an equimolar composition (Ce$_{0.5}$Zr$_{0.5}$O$_2$), while the alumina contained 4 wt% La$_2$O$_3$ [21]. Two additional samples were acquired for comparison to Pd/Al and Pd/CZO. A 1.6 wt% Pd on SASOL Puralox TH100/150 γ-Al$_2$O$_3$ without La$_2$O$_3$ (Pd/A) was described in another work [5] and used here to compare the effects of La$_2$O$_3$. Uncatalyzed Ce$_{0.5}$Zr$_{0.5}$O$_2$ (CZO) powder from Solvay was also used as a standard to acquire baseline characterization data. All powders were sieved to obtain particles between 40 and 60 mesh (250–420 μm).

2.2. Model TWC sample aging and air treatment procedures

A 1.50 g portion of catalyst powder was loaded in a quartz boat and placed inside a 19 mm ID quartz reaction tube in the heating zone of the surrounding oven. A thermocouple was placed over the boat in the aging gas stream and a second thermocouple was bent into the boat with the tip buried in the powder. The CO gas stream was scrubbed of iron carbonyls before introduction to the reactor.

Catalyst aging environments were established in a continuous flow reactor at a total flow rate of 3 L/m and heated at 700 °C for 16 h to simulate in-use drive cycle conditions at the engine-out location. The continuous redox aging gas composition contained 10% H$_2$O in N$_2$ plus alternating 10 min step pulses of lean (0.1% O$_2$) then rich (0.15% CO and 0.05% H$_2$) as shown in Fig. 1a. This environment likely kept Pd in the metallic state during the entire 16 h as with just 0.1% O$_2$ in the lean step, the aging temperature of 700 °C was well above the PdO decomposition temperature [22]. Our previous works used 2 h dry air post-aging treatments to restore lost Pd dispersion [21,22]. However in this plan, brief air treatments were inserted during the lean step pulse of the redox cycle to interrupt the deterioration caused by the previous rich step pulse. Compressed dry air at 700 °C was applied to the catalyst by replacing the redox aging gas feed for a portion x minutes of the 10 min lean pulse as shown in Fig. 1b. A 1/6 min air pulse was similar in length to an actual engine fuel cut when a vehicle slows down from highway speed [21]. Longer air pulses were used to counteract SMSI effects. Gasoline engines typically operate about the fuel/air stoichiometric ratio so the automotive catalyst OSC state is partly depleted. All catalyst samples in this work were characterized and evaluated in the reduced state by exposing them to a flow of 9% H$_2$ in Ar at 300 °C for 30 min prior to cooling in Ar to room temperature.

2.3. Catalyst characterization techniques

Structural characterization was performed with powder X-ray diffraction (XRD) pattern analysis. The instrument used for pattern acquisition was a Rigaku Miniflex II diffractometer with Cu Kα X-Ray radiation source (λ = 1.5406 Å) operating at 30 kV and 15 mA.

A catalyst sample mass of 0.1 g was wet-milled with a mortar and pestle in ethanol, then pipetted onto an off-axis-cut silicon sample holder and dried. Scans were collected with a step size of 0.005°2θ at 1°2θ/min. Phase identification and lattice parameter refinement was completed using Rigaku PDXL 2 and MDI Jade 2010 software.

The surface characteristics of the catalysts were determined by N_2 physisorption, Diffuse Reflectance Infrared Fourier Transform Spectroscopy (DRIFTS) and X-ray photoelectron spectroscopy (XPS). The Brunauer–Emmett–Teller (BET) specific surface area and Barrett, Joyner and Halenda (BJH) pore volume (for pores between 17 and 300 Å) were determined with a Micromeritics ASAP2420 instrument using N_2 adsorption at 77 K. A 48-point adsorption and 33-point desorption isotherm plot was generated across a range of 0.1-0.9 P/P₀. Infrared spectra were collected with a Nicolet 6700 FTIR spectrometer with Auxiliary Experiment Module including a praying mantis cell to facilitate gas exchange to and heating of the sample. Fine powder catalyst samples recovered from the XRD sample holder were poured into the praying mantis sample cup onto a supporting screen. The IR spectra were collected with 64 scans at a resolution of 2 cm⁻¹ repeating every two minutes. Spectra on the "as-is" samples were first obtained in N_2-only feed gas at the end of a 1 h stabilization at fixed temperatures in the range of 22 °C–400 °C, then again during a 2 h soak in 1% O_2 balance N_2 at the same temperatures for comparison. Clean sample surfaces were prepared as follows: 1) 25% H_2 in nitrogen fed at 0.2 L/m for 16 h at 400 °C, 2) added 0.8 L/m N_2, switched off H_2 and waited for 10 min to purge, 3) added 1% O_2 to the nitrogen carrier gas to burn off saturated carbonates and formates for an hour, 4) switched off O_2 and waited for 10 min to purge, and 5) heated the sample cell to 600 °C for one hour in nitrogen-only to decompose surface PdO. A clean sample background was acquired first under flowing nitrogen in stabilized temperature intervals from 400 °C to 22 °C. After the clean spectra at 22 °C were collected, 1% CO was added for two hours to saturate the surface while spectra were collected. Elemental composition and chemical state information were determined with a Kratos AXIS 165 Electron Spectrometer using a monochromatic Al Kα X-ray excitation source (1486.6 eV) operated at 12 kV, 20 mA (240 W). Each sample was pressed into a pellet and then mounted onto sticky double sided pressure sensitive adhesive tape. Data was collected using pass energies of 80 eV or 20 eV to collect survey or high resolution spectra, respectively. All spectra were acquired using charge neutralization with an electron flood source. Elemental quantification of the high resolution spectra was accomplished using CASAXPS software, using routines based on Scofield photoionization cross-section values. A Shirley type background was used to fit all high resolution spectra. For Pd on alumina support, the high resolution Pd 3d spectra was fit with a doublet using 60% Gaussian and 40% Lorentzian line shapes with an area ratio of 0.667, a full width at half-maximum (FWHM) constrained within 0.6–2.8, and a peak separation of 5.2 eV. For Pd on CZO support, the Zr 3p fit was first determined from a CZO standard using 60% Gaussian and 40% Lorentzian line shapes with an area ratio of 0.5, a FWHM constrained between 0.6 and 2.8, and a peak separation of 13.4 eV. The remaining area under the envelope was then fit by adding Pd 3d peaks using the fitting parameters described above for Pd on alumina. Binding energies were referenced to the aliphatic C 1s peak at 284.6 eV [25]. The thickness of a ceria overlayer on a model atomically flat Pd surface was calculated using the full substrate overlayer model below [25].

$$\left(\frac{I_{ov}}{I_{sub}}\right) = \left(\frac{SF_{ov}}{SF_{sub}}\right)\left(\frac{\rho_{ov}}{\rho_{sub}}\right)\left(\frac{1 - e^{-d_{ov}/\lambda_{ov}sin\phi}}{e^{-d_{ov}/\lambda_{sub}sin\phi}}\right) \tag{1}$$

In Eq. (1), I_{ov} and I_{sub} are the integrated intensities of the element of interest in the overlayer and substrate, respectively, SF_{ov} is the instrument sensitivity factor for the element of interest in the substrate at 16.0, ρ_{ov} is the molar density of the overlayer at 0.044 mol/cm³, ρ_{sub} is the molar density of the substrate at 0.112 mol/cm³, d_{ov} is the thickness of the overlayer, λ_{ov} and λ_{sub} are the inelastic mean free paths (IMFP) of the element of interest in the overlayer and substrate, respectively, and ϕ is the take-off angle (45°). IMFP was calculated according to the TPP-2M predictive formula [26], and IMFP values of Pd 3d and Ce 3d are 1.4 nm and 1.2 nm, respectively.

Pd particle size estimates were performed using XRD peak fitting by and H_2 chemisorption. These are complimentary because XRD Pd size estimate is a volumetric average technique that measures crystallite length regardless if the particles are covered by support, while chemisorption is a surface average technique that will not detect support-covered metal particles. Both techniques average size calculations are weighted towards larger particles.

A single-peak curve fitting analysis of the XRD pattern Pd peak for mean Pd crystalline length was performed using the Scherrer equation [27]. The shape factor used was 0.89 for spherical crystallites and the peak integral method was used to determine peak breadth. The instrument broadening was corrected with a LaB₆ calibration standard. Scherrer crystallite size provides a bulk average estimate of the Pd crystallite length, which may be analogous to the Pd particle size as was demonstrated for metal particles in the size range of 2–33 nm when electron microscopy and chemisorption were also used for confirmation [28–31]. Crystallite length can be smaller than particle size if large particles are made of agglomerated crystals or if any poorly crystalline regions exist in the particle. The Pd metal dispersion (D) was estimated using Eq. (2) below as a function of the Pd particle size (d_p) determined by XRD, which is described further by Baylet et al. assuming spherical shapes [32]. In Eq. (2), M_{Pd} was the Pd atomic weight of 106.4 g/mol, ρ_{Pd} was the Pd density of 12 g/cm³, and S_{Pd} was the Pd metal molar surface area of 47,780 m²/mol assuming an equidistribution of the low index faces.

$$D[\%] = (6 \times 10^5) * (M_{Pd})/(\rho_{Pd} * S_{Pd} * d_p[nm]) \tag{2}$$

H_2 chemisorption was performed using a Micromeritics ASAP2020 instrument with a static volumetric adsorption/outgas/re-adsorption method described by Chen et al. [5]. Prior to analysis, each sample was first degassed in N_2 at 500 °C, reduced at 350 °C in pure H_2, exposed to vacuum at 1 microtorr and finally dosed with H_2 at 35 °C for chemisorption measurements using a 5-point isotherm extrapolated to zero pressure. A hydrogen adsorption stoichiometry value of 1 was assumed for one adsorbed H atom per every one surface Pd atom. The differential results were used to report Pd dispersion and size to exclude physisorbed H_2 on the support. This technique is an improvement upon the classic H_2–O_2 titration method and avoids problems of H_2 spill-over and Pd hydride formation from interfering with the irreversible adsorbed H_2 calculation [33,34]. H_2 chemisorption was used for all samples since CO chemisorption tests significantly overestimated the Pd dispersion on the CZO supports, likely due to CO adsorption on CZO forming stable carbonate species [35].

Microscopy images were acquired with a FEI Talos F200X high-resolution scanning transmission electron microscope (STEM). The STEM High Angle Annular Dark Field (HAADF) image resolution was 0.16 nm. The Schottky field emission gun was set to 200 keV acceleration voltage. Samples for imaging were prepared by dispersing 10 mg of catalyst sample powder in 2 mL of ethanol followed by ultrasonification for one hour to make a suspension, then dripped onto a 200-mesh carbon coated copper grid and dried. The size of a Pd particle was determined by measurement of the imaged particle diameter once along the longest width and again along the shortest width, and then the two results were averaged. Isolated Pd particles were counted while agglomerates of several Pd particles

were ignored and no attempt was made to perform a deconvolution of overlapping 2D circular Pd images. Bruker Esprit software was used with energy dispersive X-ray spectroscopy (EDS) hyperspectral mapping, which stores a spectrum at every pixel to positively identify Pd particles, and extract spectra from the data cube of the elements present in specific areas of interest in the STEM image.

2.4. Catalyst activity measurements

A flow reactor was used to enable measurement of CO_2 formed by probe reaction tests on a characterized catalyst sample. The ASAP2020 quartz j-tube and sample used in the H_2 chemisorption test was fit onto the flow reactor. The j-tube measured 10.5 mm ID and a catalyst sample mass of 0.30 g was loaded between redistributing layers of quartz wool. The catalyst bed height was 4 mm for the Pd/CZO samples and 6 mm for Pd/Al and Pd/A samples. Matheson dynablenders and flow controllers managed the gas flow through the system. The gas stream could be triggered to route through a water bubbler and lines were maintained at 150 °C to limit condensation. The CO gas stream was scrubbed of iron carbonyls. Two K-type 1/32-in. diameter thermocouples were placed 16 mm before and 13 mm after the sample bed. A Hiden HPR20 quadrupole electron ionization mass spectrometer with Secondary Electron Multiplier (SEM) detector measured five configurable mass values in the outlet gas stream. It had a 2 Hz sampling rate at an inlet sampling pressure of 1×10^{-5} Torr and required two post-processing data corrections. First, the double excitation argon (Ar) mass 20 value was scanned, which is 11% of the total Ar level, rather than the typical mass 40 to get the measured Ar value below the SEM detector limit of 1×10^{-6} Torr. Second, there was a CO and CO_2 mass overlap of 11.4%, so that amount of the CO_2 value was subtracted from the CO value. OSC measurements were run by alternating one minute lean or rich square step pulses, each separated by a one minute purge. The purge pulse was 2% CO_2 in Ar at 975 mL/min. The lean pulse was 1% O_2, 2% CO_2 in Ar at 1 L/m and the rich pulse was 2% CO, 2% CO_2 in Ar at 1 L/min. At least five CO pulses were measured in each 50 °C increment, starting at 50 °C and ending at 400 °C. The WGS and CO light-off measurements were run with a constant feed at 1 L/min. The WGS feed was 2% CO, 2% CO_2, 2.5% H_2O and balance Ar. The CO light-off feed was 2% CO, 2% CO_2, 1% O_2 and balance Ar. The WGS and light-off gas mixtures were initially established at equilibrium over the catalyst sample at 30 °C, then the oven heating ramp was triggered at 10 °C/m to 400 °C. A special step was required for Pd/CZO samples on the CO light-off test to prevent oxidation at a 30 °C inlet temperature driven primarily by support oxidation with gas phase oxygen since the catalysts were initially reduced; CO was not introduced until the temperature rise from reoxidized CZO was cooled back down to room temperature.

3. Results

3.1. Support phase identification

The XRD patterns of the redox aged and air treated Pd model catalyst samples are shown in Fig. 2. The XRD patterns are consistent with the expected peaks for CZO in Fig. 2a, and Al_2O_3 support in Fig. 2b and c. In Fig. 2a, no CZO phase separation was evident after 16 h of exposure to the 700 °C redox aging environment. Pd [111] peaks were observed at 40°2θ for all redox aged Pd/CZO samples. The redox aged samples with air pulse length of 0–1 min also had smaller Pd peaks of [200] at 46°2θ and [220] at 68°2θ in the shoulders of the CZO support peaks. The air pulse length of 2–10 min decreased the area of the Pd peaks, indicating Pd particle redispersion. Additionally, the Pd peaks were shifted to lower scattering angles, indicating an expanded Pd crystal lattice. The Pd lattice

expansion from the redox aged sample to the 2–10 min air pulse samples was 3% as shown in Fig. 2d and in Table S1. In Fig. 2b and c, the Al_2O_3 support peaks obscured all the Pd peaks, except the Pd [311] peak at 82°2θ. No significant changes to the lattice parameter were evident in either support materials due to aging or air pulse duration. In Fig. 2b, the 1/6 min and 1 min air pulses all showed decreased Pd peak intensities and Pd peaks shifted to lower scattering angles, relative to the continuous redox aged sample, indicating that Pd redispersion occurred. The Pd lattice expansion from the redox aged sample to the 1 min air pulse sample was 3% as shown in Fig. 2d and in Table S2. These results suggest that Pd redispersion was more restricted on the CZO support compared to the Al support. In Fig. 2c, the Pd [311] peak did not decrease or shift with 1/6 min air pulses, indicating that no Pd redispersion occurred.

3.2. Catalyst characterization

The surface area and pore volume for each sample are listed in Table 1. The fresh Pd/CZO catalyst had a surface area of 91 m^2/g and redox aging with or without air pulses sintered the surface area by 53–58%. The fresh Pd/Al catalyst (Pd on 4 wt% La_2O_3 stabilized γ-Al_2O_3) had a surface area of 209 m^2/g and redox aging with or without air pulses sintered the surface area by 23–26%. The fresh Pd/A catalyst (Pd on γ-Al_2O_3) had a surface area of 138 m^2/g and redox aging with or without air pulses sintered the surface area by 15–18%. Therefore replacement of lean pulse portions with air did not show much of an effect on the surface area of these supports. All of the aged samples had a pore volume similar to their fresh state, thereby ruling out support pore structure collapse or pore blockage as playing a role in our results.

The apparent Pd particle size (d_p) and Pd dispersion (D) for each sample are listed in Table 1. Redox aging caused SMSI effects that resulted in large disagreements between H_2 chemisorption and XRD results on the Pd/CZO and Pd/Al samples, but not on the Pd/A samples. SMSI effects can cause inaccuracies in the H_2 chemisorption results, due to the support La_2O_3 electronically coupling with the Pd metal [19,20] or Ce_2O_3 covering the Pd surface [13–15], which cause lower adsorbate gas chemisorption with the Pd metal. These SMSI effects can be reversed by sufficiently long post-aging oxidation treatments [13,21,22] and Ce_2O_3 decomposition from the surface [13,36]. While two hour air post aging treatments were studied in our previous works [21,22], the focus of this study will be on using shorter air pulses to interrupt the redox aging deterioration to achieve Pd size reductions on smaller Pd particles.

The Pd/CZO sample series listed in Table 1 had undetectable (u/d) H_2 chemisorption results suggesting decoration of Pd by the support oxide after aging that was gradually removed by longer air pulses. The fresh Pd/CZO sample #1 had Pd particles that were too small to be observed with an XRD pattern fit, but these particles were detected by H_2 chemisorption to have a bulk size of 5.1 nm in diameter for a dispersion of 21%. Continuous redox aging on Pd/CZO sample #2 sintered the Pd particles to an average size of 21 nm by XRD measurement. The air pulses used during redox aging on Pd/CZO samples #3 through #5 lacked sufficient time to counteract SMSI support coverage that enables apparent Pd redispersion into smaller particles [21,22]. Therefore brief isolated fuel cuts of 1/6 min during vehicle operation may not be effective for maintaining small Pd size on this support. The redox aged sample #6 interrupted by 10 min air pulses exhibited a Pd size reduction to 8.0 nm by XRD measurement, which was near the fresh 5.1 nm Pd size as measured by H_2 chemisorption, although a 3.2% dispersion result by H_2 chemisorption for sample #6 is well below the 14% dispersion result by XRD likely due to some residual CZO support oxide decoration of Pd.

The Pd/Al sample series listed in Table 1 exhibited an interaction between Pd and the support oxide after aging as shown
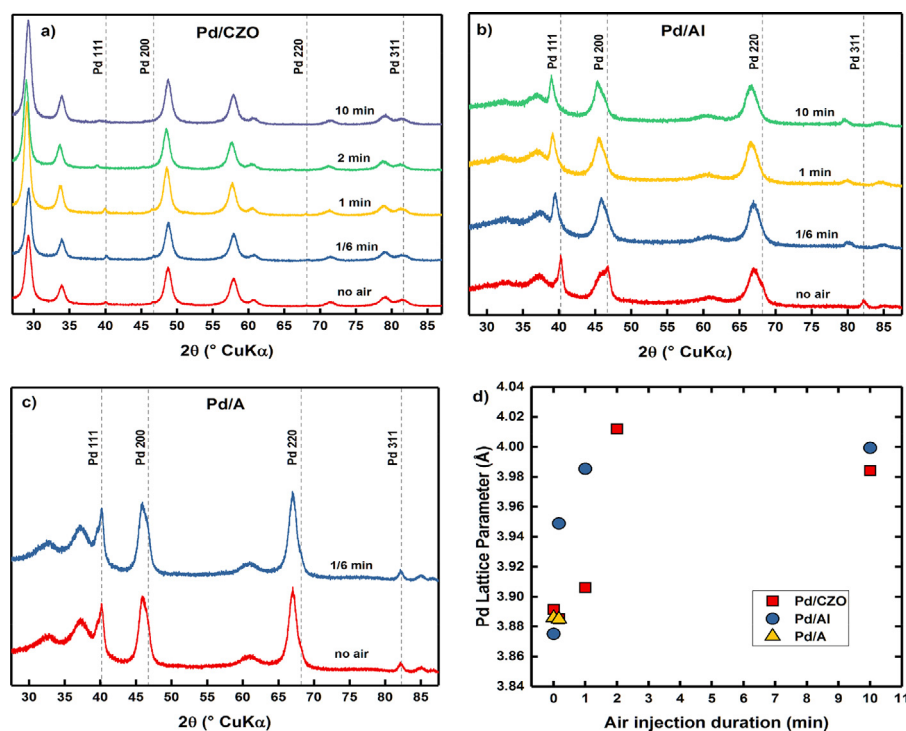
Fig. 2. XRD patterns of Pd model catalysts. Plots: a) Pd/CZO, b) Pd/Al, c) Pd/A, d) Pd lattice parameters.

Table 1
Catalyst samples and characterization results.

| Samples		Duration of air pulse x [m]	Surface area [m²/g]	Pore volume [cm³/g]	H₂ Chemisorption		XRD Pd peak fit	
ID#	Condition				d_p [nm]	D [%]	d_p [nm]	D [%]
1	Pd/CZO fresh	–	91	0.16	5.1 nm	21%	u/d*	u/d*
2	Pd/CZO redox aged (10 m rich/x m	0	41	0.15	u/d†	u/d†	21 nm	5.4%
3	air/10 m lean − x m)	1/6	38	0.15	u/d†	u/d†	28 nm	3.9%
4		1	38	0.15	u/d†	u/d†	25 nm	4.4%
5		2	40	0.15	90 nm†	1.2%†	17 nm	6.4%
6		10	43	0.15	35 nm†	3.2%†	8 nm	14%
7	Pd/Al fresh	–	209	0.58	12 nm	9.1%	14 nm	7.9%
8	Pd/Al redox aged (10 m rich/x m	0	154	0.52	433 nm†	0.3%†	18 nm	6.3%
9	air/10 m lean − x m)	1/6	161	0.54	43 nm†	2.6%†	10 nm	11%
10		1	157	0.54	37 nm†	3.0%†	10 nm	11%
11		10	157	0.54	23 nm†	4.9%†	11 nm	10%
12	Pd/A fresh	–	138	0.75	11 nm	10%	10 nm	11%
13	Pd/A redox aged (10 m rich/x m	0	113	0.76	22 nm	5.0%	16 nm	7.0%
14	air/10 m lean − x m)	1/6	117	0.78	23 nm	4.9%	15 nm	7.1%

u/d = undetectable.
* No XRD pattern Pd peak.
† Pd particles suspected to be affected by SMSI.

by the large disagreement between H₂ chemisorption and XRD results. The fresh Pd/Al sample #7 (Pd on 4 wt% La₂O₃ stabilized γ-Al₂O₃) had Pd particles that were detected by H₂ chemisorption to have a bulk size of 12 nm in diameter for a dispersion of 9.1%, in reasonable agreement with the XRD measurement of 14 nm for a dispersion of 7.9%. Continuous redox aging on Pd/Al sample #8 sintered the Pd particles to an average size of 18 nm by XRD measurement yet 433 nm by H₂ chemisorption. Pd/Al sample #9 with aging interrupted by 1/6 min air pulses had a bulk Pd size of 10 nm as measured by XRD and 43 nm by H₂ chemisorption. The samples with aging interrupted by longer air pulses showed no additional benefit over the 1/6 min air pulse by XRD measurement, but showed diminishing returns for counteracting SMSI effects detected by H₂ chemisorption. The 1/6 min air pulse appeared much more effective at reversing SMSI effects and redispersing the Pd on the Al support than on CZO, and achieved about the same bulk Pd size on Pd/Al

as with the 10 min air pulse on redox aged Pd/CZO. These results suggest that SMSI electronic effects between Pd-La₂O₃ on Al₂O₃ were much faster to uncouple upon oxidation than SMSI decoration effects from CZO on the Pd surface to enable Pd redispersion on the time scale of a common engine ~10 s fuel cut.

The Pd/A sample series listed in Table 1 did not exhibit SMSI effects. The fresh Pd/A sample #12 (Pd on γ-Al₂O₃) had Pd particles that were detected by H₂ chemisorption to have a bulk size of 11 nm in diameter for a dispersion of 10%, in good agreement with the XRD measurement of 10 nm for a dispersion of 11%. The continuous redox aged Pd/A sample #13 also showed good agreement between H₂ chemisorption and XRD results. Pd/A sample #14 with aging interrupted by 1/6 min air pulses had a bulk Pd size of 16 nm as measured by XRD yet showed no change in Pd size relative to the continuous redox aged sample #13 in Table 1. The support oxides that caused SMSI effects on the other two supports may be required
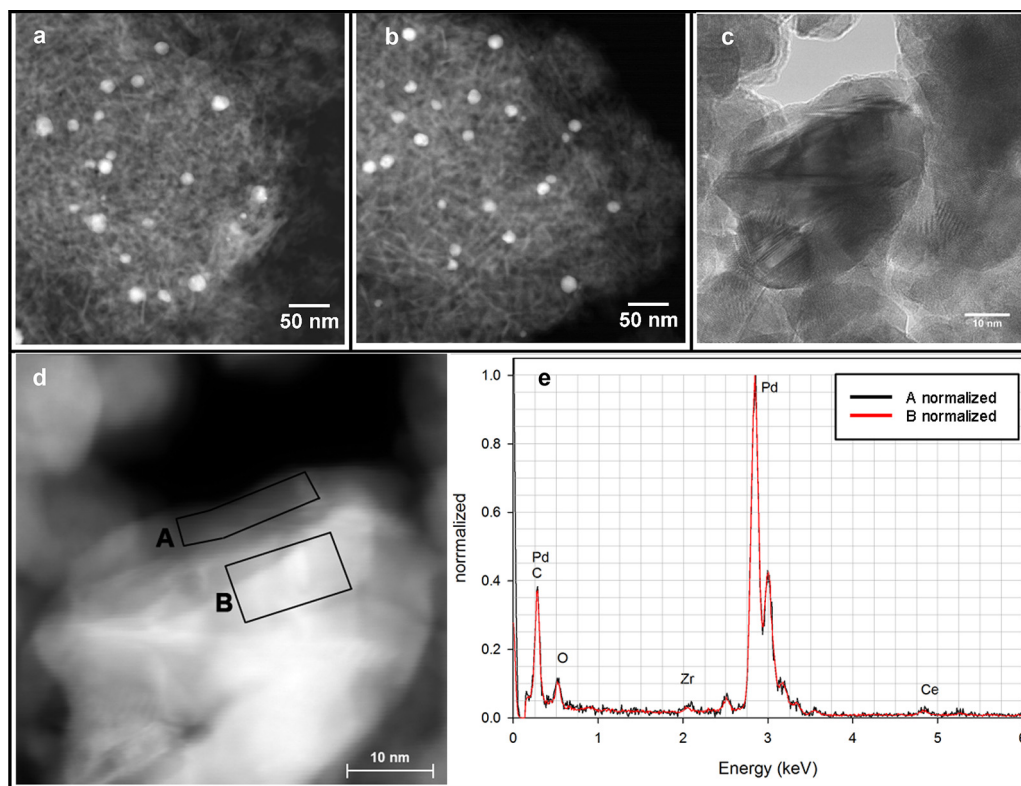
Fig. 3. STEM images of aged samples: a) Pd/Al redox, b) Pd/Al redox w/1/6 m air, c) Pd/CZO redox (bright field), d) Pd/CZO redox (dark field). EDS spectra taken from Pd/CZO redox: e) areas A and B in image d.

to assist formation of Pd^{2+} and the ensuing redispersion. Therefore brief isolated fuel cuts of 10 s in length during vehicle operation may not be effective for maintaining small Pd size on this support.

3.3. STEM characterization

STEM images from redox aged Pd/Al and Pd/CZO samples are shown in Fig. 3. Fig. 3a shows an image of the Pd/Al sample #8 that was redox aged continuously. The Pd particles shown in the dark field are bright and appear to be roughly circular in shape given the 2D image. These Pd particles are clearly an order of magnitude less than the 433 nm bulk average that was determined by H_2 chemisorption and are more in line with the 18 nm bulk average as determined by XRD. Fig. 3b shows an image of the Pd/Al sample #9 that was redox aged with interrupting 1/6 min air pulses. There did not appear to be a great reduction in Pd particle size from sample #8 to #9 as was determined by H_2 chemisorption. The air pulses during redox aging did not contribute to the formation of hollow Pd particles as was observed earlier with post-aging air treatments [21]. Fig. 3c shows a bright field image of a large Pd particle supported by multiple CZO particles from Pd/CZO sample #2 that was redox aged continuously. The top edge of the Pd particle is exposed to a pore, and the irregular darkness within the particle indicates that it is not a single crystal but has multiple domains. Rounded facets appear on all particles. Ce, Zr and Pd all have a similar atomic number and hence appear mostly indistinguishable in the image, and Pd particles required identification by low magnification hyperspectral EDS mapping. Fig. 3d is the dark field image acquired with a high magnification hyperspectral EDS map. The spectra A and B in Fig. 3e are from the map data cube at the respective areas A and B outlined in Fig. 3d, and exclude bulk CZO support material: A) the wedge-shaped edge of the Pd next to a pore and B) the interior of the large Pd crystallite. Fig. 3e shows the detected elements by EDS normalized to the Pd $L\alpha$ peak (2.84 keV). The amount of Ce + Zr

relative to O is similar to the bulk CZO composition ($Ce_{0.5}Zr_{0.5}O_2$). The sum of these detected CZO components relative to Pd is about 10–15% for both areas, which is the expected relative amount for a thin film of CZO around a large Pd particle. However, area A along the particle edge had less Pd thickness than interior area B yet showed only a slight increase in Ce, Zr or O when normalized to Pd, so these detected CZO signals were likely from fluorescence of the surrounding bulk CZO material.

The counted Pd particles on each Pd/Al sample are shown as histogram bar charts in Fig. 4 with a cumulative percent line and the number average Pd particle size listed. The histogram x-axis bins are labeled at the maximum value in the bin range. For example, 4 nm is the counted particles in the 2–4 nm range. The fresh sample results were acquired in our earlier work [21]. Most of the fresh particles were in the 2–6 nm range, but about 20% were at 8 nm and larger. The aged samples Pd particle size distribution resembled a normal probability distribution, so a statistical analysis was applicable for the aged catalysts. A confidence interval of normally distributed data contains a set of plausible values for a parameter, such as a mean, and can be stated as the following [37]:

$$CI = (t_{\alpha/2, n-1}) * (s)\sqrt{n} \qquad (3)$$

where $t_{\alpha/2, n-1}$ is the t-distribution at the critical point α with $n-1°$ of freedom, times the standard deviation of the data set (s), divided by the square root of the number of counted particles (n). Comparing one mean and examining if it is outside the confidence interval around another mean is one evaluation technique to determine if the means are statistically equivalent or not. The numerical mean of the continuously aged sample was 0.38 nm larger than the mean of the air pulse sample. The 95% confidence interval of 0.61 nm is larger than the difference of the means, so the sample means are statistically equivalent. However, the particle size distribution for the two samples appeared to change due to air pulses. The continuous aging sample had one mode around 14 nm, while the air pulse
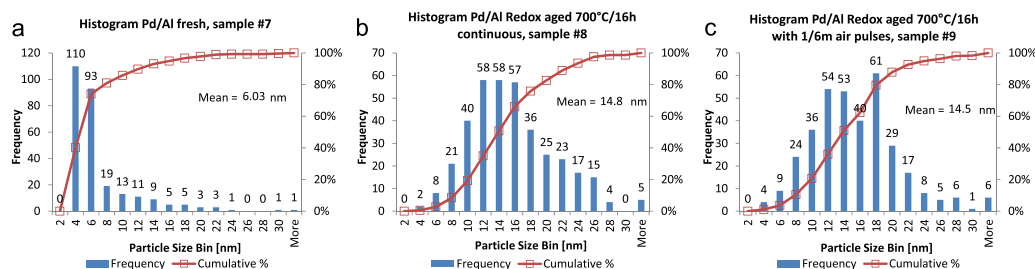
Fig. 4. Pd particle size histograms based on STEM images of Pd/Al samples. Plots: a) Fresh, b) Redox continuous, c) Redox with 1/6 m air pulses.

sample had two modes at 12 nm and 18 nm. The small particles (8 nm and smaller) were 8% of the total after continuous redox aging and increased to 10% of the total when air pulses were used. The increased small particles for the air pulse sample may have resulted from Pd redispersion. The large particles (20 nm and larger) were 17% of the total after continuous redox aging and decreased to 12% of the total when air pulses were used. The large bin at 18 nm for the air pulse sample may have resulted from the limiting of larger particle formation.

The Pd/Al sample STEM images of Pd particles with diameter, d_i, and the number of particles of a particular diameter, n_i, can be recalculated as shown by the equations below to more accurately compare against the other Pd size measurement techniques based on how those techniques determine the bulk average particle size [28]. A surface-averaged diameter is used to compare against H_2 chemisorption results while a volume-averaged diameter is used to compare against XRD results.

Number-Average	Surface-Average	Volume-Average
$d_n = \Sigma n_i d_i / \Sigma n_i$ (4)	$d_s = \Sigma n_i d_i^3 / \Sigma n_i d_i^2$ (5)	$d_v = \Sigma n_i d_i^4 / \Sigma n_i d_i^3$ (6)

Table 2 lists the number of counted Pd particles and measured average Pd diameters compared across three measurement techniques. The microscopy results verified the suspicion that SMSI effects caused the H_2 chemisorption measurement to yield artificially large Pd particle size results for samples #8 and #9. The microscopy results show that air pulses resulted in a volume-averaged Pd size of sample #9 below sample #8. The measured average Pd size by XRD is in agreement with the microscopy volume-averaged Pd size for the aged samples. The bulk average Pd size reduction measured by XRD from sample #9 relative to sample #8 appears to reflect a shift in particle size distribution away from the large particle tail (20 nm and larger in Fig. 4) rather than a shift in the overall particle size mean, since XRD results are biased towards large particles. The volume-averaged microscopy results also show that air pulses resulted in a Pd size restored to the fresh level, yet not below sample #7 as indicated by XRD. However, as 40% of the fresh Pd particles in Fig. 4a were in the 2–4 nm range, the fresh XRD value of 14 nm may be artificially high as a 6 nm crystalline length is near the detectable threshold apart from the background.

3.4. XPS surface characterization

The XPS spectra of the Pd/Al and Pd/CZO catalyst samples are shown in Fig. 5. Fig. 5a showed the Pd $3d_{5/2}$ peak at 334.8 eV ± 0.1 eV for both fresh and aged Pd/Al samples that corresponds to Pd^0 [38]. The fresh Pd/Al sample had a shoulder in the Pd $3d_{5/2}$ peak at about 336.5 eV, which was likely Pd^{2+} interface sites with the support La_2O_3 [39], but these sites were lost after aging and not restored with air pulses. The fresh Pd/A sample was evaluated in our previous work and did not show Pd^{2+} indicating the difference with La_2O_3 [21]. The La 3d and Zr 3p peaks did not show a change in

peak height or location from the fresh to aged state as shown in Fig. 5b and c, respectively. Fig. 5c showed Pd $3d_{5/2}$ peaks fit inside the shoulders of the Zr 3p peaks as is typically performed for analysis of Pd on CZO support [39–42]. Fig. 5c showed that the fresh Pd/CZO sample had two similarly sized Pd $3d_{5/2}$ peaks at 334.7 eV and 337.1 eV that corresponds to Pd^0 and Pd^{2+}, respectively [38]. The fresh Pd/CZO had an abundance of interface sites with finely dispersed Pd^{2+} and oxygen from CeO_2, but these sites were lost after aging and not restored with air pulses. No Pd peak shifting was observed due to redox aging with or without air pulses. Fig. 5d did not show a binding energy shift due to redox aging or lean treatments for the Ce $3d_{5/2}$ peak at 882.0 eV or the Ce $3d_{3/2}$ peak at 900.4 eV. The other Ce 3d peaks shown are satellite peaks that arise from interactions with the Ce 4f valence electrons after the 3d core electron is emitted.

The atomic concentrations from the top surface layers are shown in Table 3 are based on the integration of the peak intensities shown in Fig. 5. The reported values are an average of two pressed pellet samples. Adventitious carbon is formed from exposure to room temperature air during the sample transfer and pellet pressing. The observed range in concentration for the two pellets of each sample was ±0.2 at% for Ce, ±0.04 at% for La and ±0.02 at% for Pd. The fresh surface Pd concentration on CZO support was diminished by about 72% after redox aging, indicating Pd sintering plus a geometric SMSI effect of CZO coverage on Pd as Ce/Pd increased by a factor of 4. The increased air pulse length decreased the surface concentration of Ce and the Ce/Pd ratio, indicating a gradual removal of CZO from Pd with longer air pulses. The fresh Pd surface concentration on Al support was reduced by about 40% after redox aging, consistent with Pd and Al sintering from Table 1, yet did not diminish as severely as the Pd surface on CZO, since La_2O_3-Al_2O_3 is not reducible under these conditions [43] so La_2O_3 should not cover Pd. The fresh La surface concentration on Al support did not change much with aging or with air pulses. The added 1/6 min air pulse showed essentially no change in the surface La/Pd or Al/Pd concentration ratios or Pd concentration.

3.5. Infra-red measurements

The wave numbers characteristic to CO adsorption on ceria and Pd according to earlier work is shown in Table 4 [23,24,44,45–47]. The IR band wave numbers can change with temperature, pressure and CO coverage [48,49]. Therefore the wave numbers given in Table 4 are approximate.

Fig. 6 shows Pd catalyst samples after evaluation on the catalyst activity tests, which will be referred to as an "as-is" condition with carbonaceous species formed from a combination of air and CO exposure. Spectra of the adsorbed species are the difference between the absorbance of the "as-is" samples and the clean sample background. Residual carbonaceous species were observed on each support surface and no CO—Pd peaks were observed in the characteristic range of 1800–2100 cm^{-1}. In Fig. 6a for Pd/CZO, the peaks from 1000 to 1700 cm^{-1} are consistent with carboxy-

Table 2
Comparison of Pd particle diameter measured with STEM to other methods.

Pd/Al Samples		Particles Counted, n	Number-Average, d_n [nm]	Surface-Average, d_s [nm]	H_2 Chemisorption [nm]	Volume-Average, d_v [nm]	XRD [nm]
ID#	Condition						
7	Fresh	274	6.0	15.4	12	21.8	14
8	Redox 700 °C/16 h	369	14.8	20.3	433	24.5	18
9	Redox w/1/6 m air	353	14.5	19.3	43	22.4	10
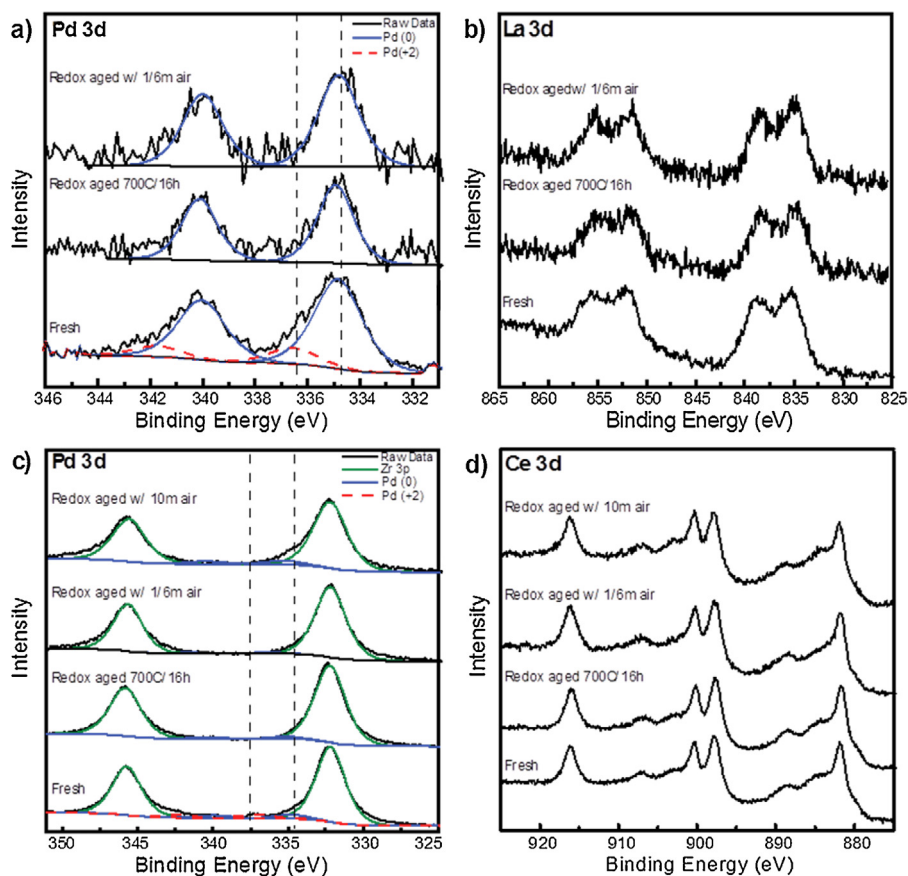
Fig. 5. XPS high resolution spectra of Pd model catalyst samples. Vertical dashed black lines indicate Pd peak centers. Solid blue lines are representative fits for Pd metal, dashed red lines are representative fits for Pd^{+2}. Spectra are offset for clarity. Plots: a) Pd 3d on Pd/Al, b) La 3d on Pd/Al, c) Pd 3d on Pd/CZO, d) Ce 3d on Pd/CZO. (For interpretation of the references to color in this figure legend, the reader is referred to the web version of this article.)

Table 3
Atomic surface concentrations of fresh and aged samples by XPS [at%].

Sample		C	O	Ce	Zr	La	Al	Pd	Ce/Pd	Al/Pd	La/Pd
Pd/CZO	Fresh	20.9	59.9	6.0	12.6	–	–	0.57	10.5	–	–
	Redox aged 700 °C/16 h	22.8	56.2	6.9	13.9	–	–	0.16	43.1	–	–
	Redox aged w/1/6 m air	34.3	48.7	5.5	11.3	–	–	0.21	26.2	–	–
	Redox aged w/2 m air	34.0	50.1	4.9	11.0	–	–	0.22	22.6	–	–
	Redox aged w/10 m air	36.0	47.4	5.2	11.2	–	–	0.31	16.8	–	–
Pd/Al	Fresh	14.5	50.7	–	–	0.24	34.3	0.20	–	172	1.2
	Redox aged 700 °C/16 h	16.4	52.7	–	–	0.30	30.6	0.12	–	266	2.5
	Redox aged w/1/6 m air	16.0	52.5	–	–	0.26	31.1	0.12	–	259	2.2

lates, carbonates and formates. Most carbonaceous species were present through at least 400 °C even under oxidizing conditions, which demonstrates their role as spectator species on the CZO support. The oxidation feed at 400 °C enhanced formation of peaks at 1230 cm^{-1} (OH bend) and 1524 cm^{-1} (N—H bend) over the N$_2$-only feed gas. In Fig. 6b for Pd/Al, the only major peaks were broad and were near 1464 cm^{-1} (C—H bend) and 1576 cm^{-1} (N—H bend).

These peaks were still present after 2 h in 1% O$_2$, which demonstrates their role as spectator species on the Al support.

Fig. 7 shows Pd catalyst samples that were preconditioned to remove carbonaceous species off from the surfaces, then thermally decomposed PdO to Pd, and then exposed to gas phase CO while IR spectra were acquired every 2 min over 2 h. Spectra of the adsorbed species are the difference between the absorbance of the CO satu-
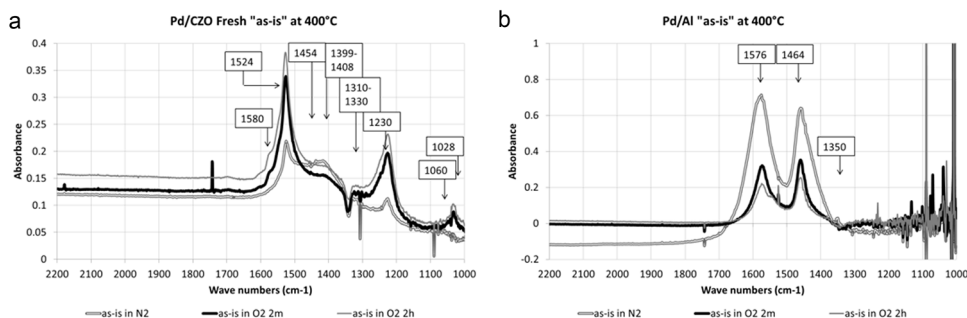
Fig. 6. IR spectra of "as-is" fresh samples at 400 °C. Plots: a) Pd/CZO, b) Pd/Al.
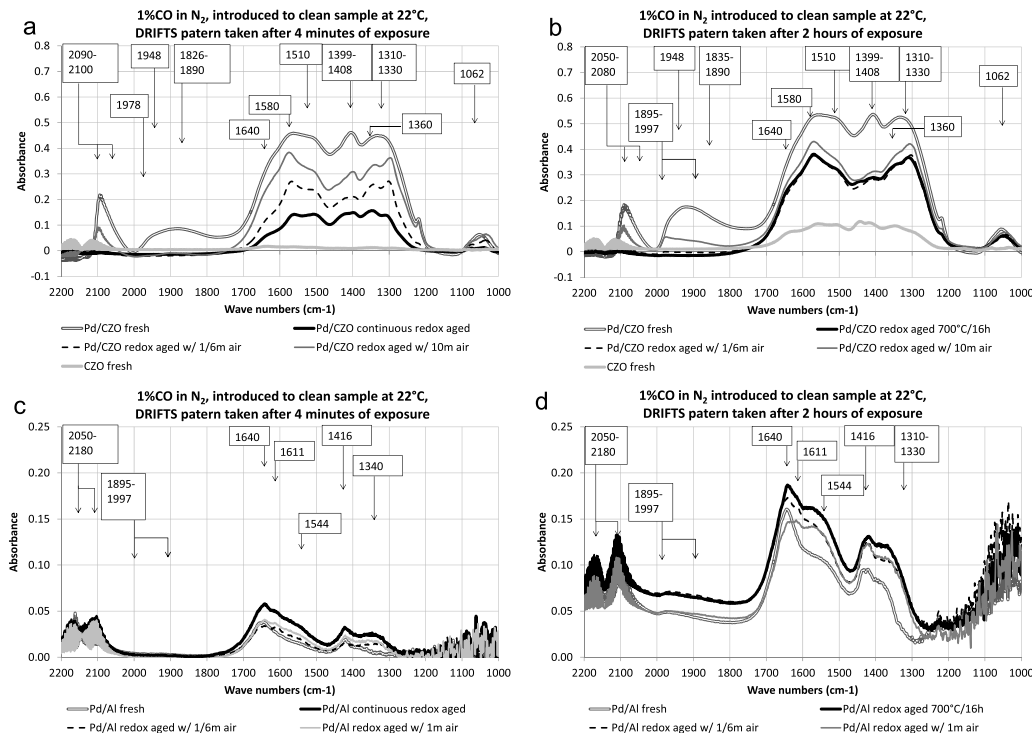

Fig. 7. IR spectra during CO exposure onto clean samples at 22 °C. Plots: a) Pd/CZO after 4 min, b) Pd/CZO after 2 h, c) Pd/Al after 4 min, d) Pd/Al after 2 h.

Table 4
Probable locations of IR bands from literature.

Species	Wave number [cm^{-1}]	References
Carbonates bidentate	1028, 1286, 1562	[44]
Carbonate unidentate	1062, 1454	[44]
C—O stretch	900–1300	[46]
CO—Ce^{+4} linear	1310–1330	[44]
OH bend	1200–1450	[46]
C—H bend	1300–1475	[46]
Formates	1360, 1580	[44]
Hydrogen carbonate	1399–1408	[45]
Inorganic carboxylate	1510, 1560	[44]
N—H bend	1500–1650	[46]
C=C stretch	1575–1700	[46]
C=O stretch	1640–1850	[46]
CO—Pd [111] bridge x3	1826–1890	[23,47]
CO—Pd [111] bridge x2	1920–948	[23,24,47]
CO—Pd [100] bridge x2	1874–1997	[23,24,47]
CO—Pd [111] on top	2050–2080	[23,24,47]

rated samples and the clean sample background. For all samples, gas phase CO appears as two similar bands starting at 2050 cm^{-1} through 2200 cm^{-1} with high frequency and low amplitude of

approximately 0.04 absorbance, which partially obscures peaks of linearly adsorbed CO on Pd[111]. In Fig. 7a, b, the peaks from 1000 to 1700 cm^{-1} are carbonaceous species consistent with carboxylates, carbonates and formates, and similar with the peaks observed for "as-is" surface condition in Fig. 6a. The growth rate of carbonaceous species showed the following trend: fresh Pd/CZO > Pd/CZO redox aged with 10 m air > Pd/CZO redox aged with 1/6 m air > Pd/CZO continuous redox aged » CZO. This large difference between uncatalyzed CZO and the Pd/CZO samples implies that Pd enhances the formation of carbonaceous species at the Pd-CZO interface or adlineation sites. In Fig. 7c, d, the carbonaceous species formed on Pd/Al showed peaks at 1340 cm^{-1} (C—H bend or OH bend) on just the aged Pd/Al samples that are suspected to have an SMSI effect with the H$_2$ chemisorption results in Table 1. There were also peaks near 1416 cm^{-1} (C—H bend) and 1544 cm^{-1} (N—H bend) that may have been the same species observed for the Pd/Al "as-is" samples in Fig. 6b. Carbonaceous species on aged Pd/Al grew as fast as on fresh Pd/Al and did not show a clear trend with aging or air pulses.

Fig. 8 shows the IR spectra range just for CO adsorbed on Pd after two hours of CO saturation. The spectra were acquired with CO turned off to avoid gas phase interference bands. In Fig. 8a,
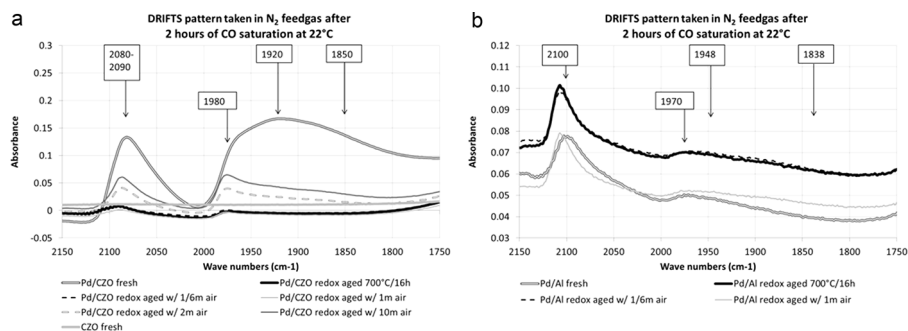
Fig. 8. IR spectra in N_2 after 2 h CO exposure at 22 °C. Plots: a) Pd/CZO, b) Pd/Al.
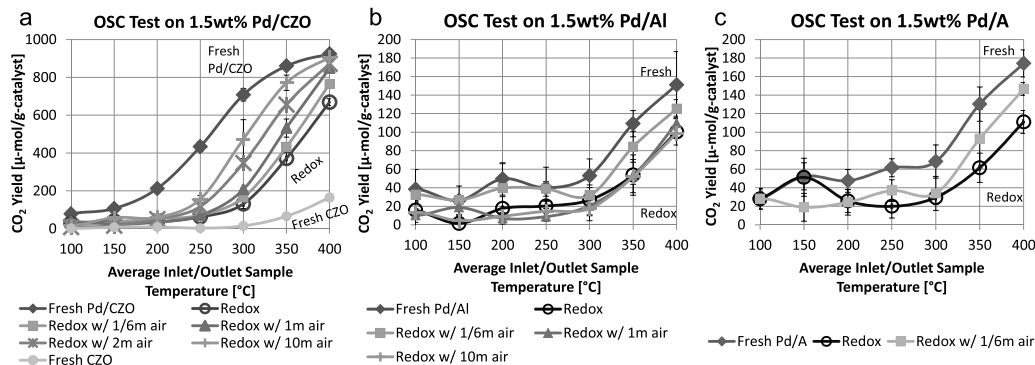

Fig. 9. OSC catalyst activity tests. Plots: a) Pd/CZO, b) Pd/Al, c) Pd/A.

fresh Pd/CZO showed multiple IR bands: a strong linear CO—Pd[111] band near 2080 cm^{-1}, a strong two-fold bridged CO-Pd [100] near 1980 cm^{-1}, a weak two-fold bridged CO—Pd[111] near 1920 cm^{-1}, and a strong three-fold bridge CO-Pd[111] band near 1850 cm^{-1}. Redox aging of Pd/CZO caused changes to the metal and support that resulted in very poor CO adsorption onto Pd facets, and only slightly more than uncatalyzed CZO. These Pd/CZO fresh and continuous redox aged results are consistent with Badri et al. for 1.2 wt% Pd on CeO$_2$ before and after reduction in H$_2$ at 600 °C [13]. The continuous redox aging along with redox aging interrupted by 1/6 min and 1 min air pulses all showed equivalent spectra, as these air pulses were not long enough to counteract the changes on the Pd/CZO surface caused by redox aging. The redox aging interrupted by 2 min and 10 min air pulses showed much more intense CO—Pd linear and bridge peaks, but were still significantly below the fresh Pd/CZO spectra. These results confirm the suspicions in Table 1 that all aged Pd/CZO samples were affected by geometric SMSI effect of support oxide coverage on Pd, only to a lesser degree with longer air pulses. In Fig. 8b, Pd/Al fresh showed similar CO adsorption onto Pd as with the redox aged samples exhibiting a linear CO—Pd[111] band near 2100 cm^{-1}, weaker two-fold bridged CO—Pd[100] and CO—Pd[111] bands near 1948 cm^{-1} and 1970 cm^{-1}, respectively, and a faint three-fold bridge CO-Pd[111] band near 1838 cm^{-1}. These Pd/Al spectra are consistent with the work by Lear et al. for CO saturation of Pd/Al$_2$O$_3$ catalysts that were each made with different Pd precursors and our Pd/Al spectra most closely matches their 1 wt% Pd(acac)$_2$ sample [50]. Pd does not appear to be covered by La$_2$O$_3$ on the aged samples, since Fig. 8b shows all samples had similar CO—Pd peak locations and intensities to fresh, but all amplitudes are almost as low as redox aged Pd/CZO. Note that the sample pretreatment conditions of 1% O$_2$ at 400 °C used to burn away saturated carbonates may also have uncoupled the La$_2$O$_3$ adducts formed during H$_2$ chemisorption as proposed by Fleisch et al. [19] from the Pd surface to allow CO adsorption on the aged samples similar to fresh.

3.6. Catalyst activity tests

Fig. 9 shows the oxygen storage capacity test results as the CO$_2$ yield for the Pd/CZO, Pd/Al and Pd/A samples. Fig. 9a shows that the aged Pd/CZO samples had a severe loss in CO$_2$ yield from fresh. Note that at 400 °C, the three highest performing Pd/CZO samples consumed the entire inlet CO pulse for the first several seconds, diminishing their CO$_2$ yield trend with increasing temperature. The 1/6 min and 1 min air pulses showed only slightly increased CO$_2$ yield over the redox aged sample at 300 °C, which aligns with the lack of exposed Pd measured by H$_2$ chemisorption for these three samples as listed in Table 1. The 2 min and 10 min air pulses showed increased CO$_2$ yield over the other aged samples at 300 °C, which is consistent with the presence of exposed Pd measured by H$_2$ chemisorption for these two samples as listed in Table 1. Fig. 9b and c shows the OSC results for the Pd/Al and Pd/A samples. La$_2$O$_3$ and Al$_2$O$_3$ had negligible oxygen mobility under these conditions and the OSC CO$_2$ yield measured during the CO step was only based upon the amount of PdO formed on the lean pulse step. There was little separation from fresh to aged so the effect of air pulses was not significant on the Pd/Al and Pd/A samples.

Fig. 10 shows the water-gas shift test results as the percent of CO$_2$ yield for the Pd/CZO, Pd/Al and Pd/A samples. Fig. 10a shows the WGS results for the Pd/CZO samples. The redox aged sample showed a severe loss in CO$_2$ yield, at 300 °C and above, compared to fresh. The 1/6 min and 1 min air pulses had only a slight increase in CO$_2$ yield over the redox aged sample. The 2 min and 10 min air pulses showed a large CO$_2$ yield increase over the other aged samples at 400 °C, since air pulses on these two samples exposed Pd by H$_2$ chemisorption as in Table 1 and CO adsorption according to Fig. 8. Fig. 10b shows the WGS results for the Pd/Al samples. The fresh Pd/Al sample had the highest CO$_2$ yield at 350 °C–400 °C while the aged samples were similar to each other. Fig. 10c shows the WGS results for the Pd/A samples. The fresh Pd/A sample had the highest CO$_2$ yield at 400 °C while the other samples were similar
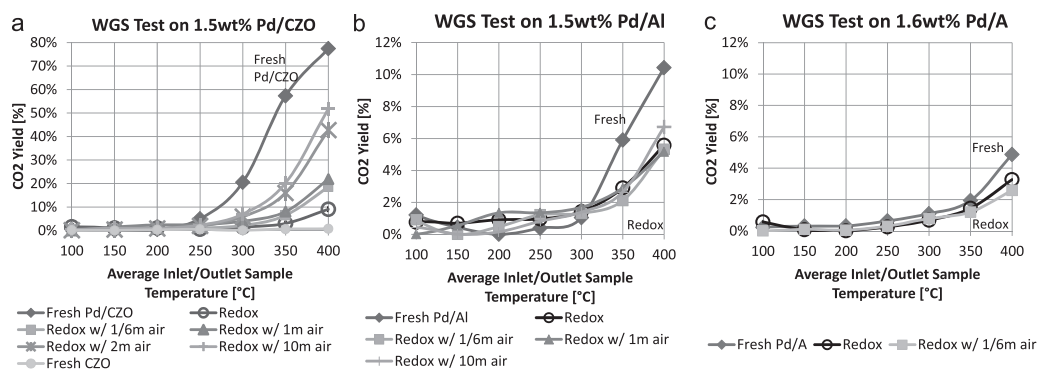
Fig. 10. WGS catalyst activity tests. Plots: a) Pd/CZO, b) Pd/Al, c) Pd/A.

to each other. The fresh Pd/Al sample had twice the CO_2 yield as the fresh Pd/A sample at 350 °C and 400 °C, in spite of roughly identical Pd dispersion measured by H_2 chemisorption in Table 1. Therefore the Pd-La$_2$O$_3$ adlineation sites on the fresh Pd/Al sample promoted WGS activity, yet did not promote significant OSC activity as shown in Fig. 9. The redox aged Pd/CZO sample had similar performance to the aged Pd/Al and Pd/A samples, indicating that redox aging disconnected the oxygen mobility from the bulk CZO to the Pd. Some oxygen mobility was restored with air pulses to increase WGS activity on Pd/CZO samples, but air pulses had no measurable effect on the Pd/Al or Pd/A samples.

Fig. 11 shows the CO light-off test results as the percent of CO_2 yield for the Pd/CZO, Pd/Al and Pd/A samples with the 50% CO conversion temperature (T_{50}) noted in the legend. In Fig. 11a, the T_{50} over Pd/CZO samples was shown to follow the following trend: fresh < with 10 m air = with 2 m air < redox < with 1/6 min air. Generally, the Pd/CZO T_{50} scaled with Pd size by XRD from Table 1 and confirms those results. In Fig. 11b, the T_{50} over Pd/Al samples was shown to be the lowest on the fresh sample and highest on the aged samples. However, the catalytic activity of all aged Pd/Al samples was much poorer than the aged Pd/CZO samples due to the difference in support oxygen mobility. The fresh Pd/Al sample T_{50} was much lower than the aged samples. All redox and air pulse Pd/Al samples had a similar T_{50} of 203 °C ± 6 °C and did not scale with Pd dispersion by H_2 chemisorption or XRD from Table 1. The fresh and aged Pd/A samples had a similar T_{50} of 208 °C ± 3 °C and did not scale with Pd dispersion by H_2 chemisorption or XRD from Table 1.

4. Discussion

4.1. Formation of Pd-SMSI effects during 700 °C redox aging

The redox aged Pd/CZO catalysts showed inhibited gas adsorption on both the CO DRIFTS and H_2 chemisorption characterization tests, which was attributed to SMSI effects through decoration of Pd by support oxide. CO adsorption onto fresh Pd/CZO in Fig. 8 showed large wide IR peaks at linear and bridge Pd—CO bonding locations, but after redox aging Pd/CZO lost nearly all IR signal intensity for CO—Pd bonding. The XPS results in Table 3 for redox aged Pd/CZO catalysts showed 15% increased surface Ce coincident with 72% decreased Pd relative to the fresh state, which was a 4 times increase in Ce/Pd from fresh to aged, while aged Pd/Al catalysts showed just a 40% decrease in surface Pd relative to the fresh state where sintering alone was expected. The prediction for ceria layer thickness described in Eq. (1) can be converted into number of monolayers where one monolayer of the ceria overlayer was defined as one complete O—Ce—O layer ($d_{ov} = 0.3$ nm). From this calculation, three ceria monolayers ($d_{ov} = 0.9$ nm) increased the Ce/Pd ratio by a factor of 4. A 0.9 nm thick overlayer is less than the IMFP of Pd 3d at 1.4 nm and Ce 3d at 1.2 nm. Therefore it is reasonable to

interpret the change in the Ce/Pd ratio reported in Table 3 as support oxide decoration of the Pd surface. While the Pd/CZO sample does not mirror this model study, the model does give an estimate of the amount of ceria needed to attenuate the observed Pd signal and shows that thicknesses significantly less than 1 IMFP can account for observed changes in the Ce/Pd ratios. Another possibility for the Ce/Pd ratio change could be Pd encapsulation by CZO where Pd is trapped under sufficient support material and can not be reoxidized [51]. However, we previously ruled out this possibility for our 700 °C aging temperature after detecting no Pd[111] peak after a treatment of air at 700 °C for 2 h using XRD on redox aged Pd/CZO samples [21]. Therefore on our aged Pd/CZO samples we suspect a thin layer of CZO support oxide decoration on Pd, rather than CZO support encapsulation of Pd. Another possibility for the Ce/Pd ratio change could be more sintering of Pd relative to Ce during redox aging. However, Ce like Al did not change by more than 20% from the fresh state to any aged state as shown in Table 3. In addition, Pd size measured by XRD after continuous redox aging was about 20 nm regardless of support material. These characterization results all align to provide indirect evidence towards confirmation that a support oxide decorated the Pd surface.

An attempt to provide direct evidence of a thin CZO support oxide layer decoration on Pd by STEM was shown in Fig. 3. A 40 nm Pd crystallite was found supported over the edge of a CZO particle that was large enough to exclude bulk CZO support from area elemental analysis by EDS. The normalized peak heights of Ce and Zr detected by EDS were each about 5% of Pd, while O was 10% of Pd, which were similar to their relative proportions in the bulk CZO material. No faceted Pd particles were observed in our Pd/CZO image, which would have enabled a direct observation of CZO layers on a Pd surface by tilting an exposed Pd facet parallel to the electron beam. The approximate 10–15% of CZO normalized to Pd seems reasonable for a roughly 0.9 nm CZO coating on a 40 nm Pd particle. Yet the difference in Pd thickness for area A and B did not show a significant difference in Ce, Zr or O when normalized, so some contribution from local x-ray scatter cannot be ruled out. High-resolution transmission electron microscopy work by Gatica et al. on samples of 0.53 wt% Pd on Ce$_{0.68}$Zr$_{0.32}$O$_2$ also could not detect Pd decoration by the support oxide after a 5% H_2/Ar reduction held at 700 °C for 1 h [52]. These efforts highlight the difficulty in using microscopy to directly confirm a thin film of CZO decoration on Pd when CZO is the bulk support material.

The OSC and WGS catalyst activity tests provided complementary evidence for SMSI effects on CO oxidation through decoration of Pd by CZO support oxide. For Pd/A catalysts on the OSC test, the lean step saturates the support and metal surface with oxygen then on the rich step CO adsorbs onto PdO where it reacts into CO_2 and desorbs. Fresh Pd/CZO catalysts have an additional reaction route of oxygen supplied from the support to react adsorbed
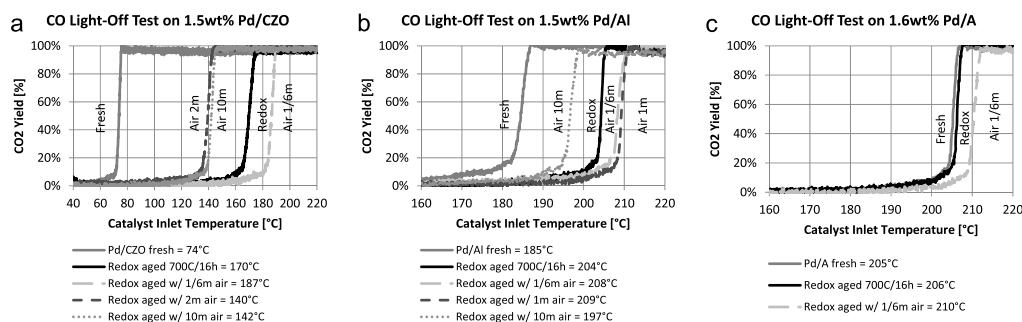
Fig. 11. CO light-off catalyst activity tests. Plots: a) Pd/CZO, b) Pd/Al, c) Pd/A.

CO into CO_2 while the support oxygen vacancy is refilled on the following lean step with gas phase oxygen. From Fig. 9 at 300 °C, fresh PdO on CZO with excellent oxygen mobility had over 10 times more OSC CO_2 yield than fresh PdO on an inert alumina support, but after redox aging the performance of Pd/CZO significantly degraded towards that of the inert supports at just 4 times more OSC than aged Pd/A. Therefore, the metal-support interface of CZO decorated Pd particles would likely have more restricted capability to transfer oxygen to Pd. The WGS test associative mechanism involves CO adsorption onto Pd coupled with water decomposition at the interface so that CO and OH react into CO_2 and H. The WGS redox mechanism also involves CO adsorption onto Pd, but oxygen is supplied from the support at the metal interface to react CO into CO_2 while the support oxygen vacancy is refilled by water decomposition. Fresh Pd/CZO can use both mechanisms since the support has O_2 mobility, while Pd/A can use only the associative mechanism since the support is inert. From Fig. 10, the WGS conversion at 400 °C for fresh Pd/CZO was 77% and fresh Pd/A was 5%, after redox aging, Pd/CZO was 9% and Pd/A was 3%. Fig. 10a shows the WGS conversion for fresh CZO was near 0% at 400 °C as this reaction requires a metal-support interface. The CZO decorated Pd sites performed similarly to redox aged Pd-Al_2O_3 sites on the WGS test, with both demonstrating poor O_2 mobility from water decomposition. Together, SMSI effects observed on Pd/CZO were a detriment to CO oxidation with poor gas phase adsorption leading to poor interaction with reactants and a lack of oxygen supply from the support.

The continuously redox aged Pd/Al catalyst showed inhibited gas adsorption on the H_2 chemisorption characterization test. In the literature, Pd-La_2O_3 geometric SMSI effects were generally proposed when 1) the Pd dispersion results by H_2 chemisorption or H_2-O_2 titration methods were much lower for Pd supported on La_2O_3 than on SiO_2 [17–19,24], or 2) the Pd dispersion on Pd-La_2O_3-SiO_2 samples measured by the H_2 chemisorption method were much lower than when measured by a different method [53], or 3) the CO—Pd IR peak intensity for Pd-La_2O_3-SiO_2 samples were reduced compared to Pd-SiO_2 [53,54]. This geometric SMSI effect, as proposed by Fleisch et al., begins when reduced La_2O_3 species migrate onto Pd-H sites and form adducts of $LaPd_xO$ in patches on the Pd surface [19]. In our work, redox aging of fresh Pd/Al showed a large drop in Pd dispersion by the H_2 chemisorption method in Table 1 coupled with the H_2 chemisorption result being far below the XRD result in agreement with the literature. Alternatively Pd and Al_2O_3 sintering coupled with La_2O_3 surface richening near Pd may cause the Pd to behave as if supported on La_2O_3 and exhibit just electronic SMSI effects. Interrupting redox aging with air pulses revealed a large increase in Pd dispersion by H_2 chemisorption in Table 1, which may indicate that oxidation reversed the decoration of La_2O_3 onto Pd, but since XRD also showed a Pd dispersion increase, it is likely that Pd redispersion also occurred. In addition, XPS revealed that air pulses caused no such large increase in sur-

Table 5
Comparison of Pd binding energy on various supports.

Catalyst	Pd $3d_{5/2}$ Binding Energy	Reference
Pd foil	334.9 eV	[38,59]
1.6 wt% Pd on Al_2O_3 (Pd/A)	334.5 eV	[21]
6.8 wt% Pd on Al_2O_3	334.9 eV	[38]
5.0 wt% Pd on Al_2O_3	334.9 eV	[60]
1.5 wt% Pd on 4 wt% La_2O_3 doped Al_2O_3 (Pd/Al)	334.8 eV	This work
1.9 wt% Pd on La_2O_3	334.7 eV	[19]
5 Å thick film of Pd on 10 Å thick film of La_2O_3	334.9 eV	[55]
2.0 wt% Pd on SiO_2	335.3 eV	[19]
1.0 wt% Pd on 1.3 wt% La_2O_3 doped SiO_2	335.4 eV	[58]
1.0 wt% Pd on SiO_2	335.9 eV	[58]

face Pd at the expense of La in Table 2 that would be required if La was removed from on top of Pd. Our CO saturation DRIFTS results also did not support claims of geometric SMSI effects as fresh and aged Pd/Al samples had CO-Pd peaks that were similar in height and position corresponding to similar access to all Pd facets. In addition, other works cast doubt upon formation of reduced La_2O_3 species: 1) Shelef et al. showed XPS work with a thin film of Pd-La_2O_3 exposed to H_2 at 600 °C that lacked reduced surface La_2O_3 [55], 2) Yang et al. conducted H_2 reduction work through 700 °C on Pd-La_2O_3-Al_2O_3 and showed no added consumption beyond that of Pd-Al_2O_3 [43], and 3) Seoane et al. repeated H_2 reduction work through 700 °C separated by a 500 °C oxidation step in air on Pd-La_2O_3-SiO_2 and showed no added H_2 consumption beyond that of Pd-SiO_2 [53]. Room temperature CO saturation DRIFTS results by Gaudet et al. showed similar IR peak locations for 2.5wt%Pd on both 3wt%La_2O_3 stabilized γ-Al_2O_3 and γ-Al_2O_3 supports, while their La_2O_3 containing catalyst showed reduced linear CO-Pd peak height, they explained it as the result of stable Pd-O sites that diminished the number of Pd sites for room temperature CO adsorption [56]. Our XPS results with fresh Pd/Al also showed a significant stable PdO concentration that resisted a mild ex-situ reduction treatment prior to analysis, which was not present in our earlier XPS spectra work for the fresh La_2O_3-free Pd/A support [21]. Our observed Pd-La_2O_3 SMSI effects may be explained by geometric effects or stable Pd-O sites, but may also only present during H_2 chemisorption conditions and quickly reverse upon exposure to ambient air during sample transfer so as to be undetectable by our XPS, DRIFTS and catalyst activity methods. Therefore, apparent literature Pd-La_2O_3 geometric SMSI effects may be better explained by electronic effects or stable Pd—O sites. In the literature, Pd-La_2O_3 electronic SMSI effects were claimed when the Pd $3d_{5/2}$ binding energy on La_2O_3 was more electronegative (-0.7 eV) than Pd on SiO_2 or Pd^0 foil [19,20] or the reaction product selectivity increased for Pd-La_2O_3-SiO_2 versus Pd-SiO_2 [57,58]. The XPS results in Fig. 5a showed that the Pd $3d_{5/2}$ binding energy for the fresh Pd/Al did not shift after redox aging in spite of the SMSI effects shown in Table 1. Table 5 lists Pd $3d_{5/2}$ binding energies

for our catalysts and Pd foil and for those reported in the literature for similar catalysts after reduction [19,21,38,55,58–60]. The literature catalysts that contained SiO_2 exhibited Pd $3d_{5/2}$ binding energies, from 335.3 eV to 335.9 eV, that were higher than our Pd/Al and Pd/A catalysts, perhaps confirming the electronic SMSI effect as others have claimed. Yet our results for Pd/Al and Pd/A were consistent with those reported for Pd foil, Pd/Al$_2$O$_3$, Pd/La$_2$O$_3$ and Pd/La$_2$O$_3$-Al$_2$O$_3$, which exhibited a range of values from 334.5 eV to 334.9 eV. Therefore it would be difficult to conclude an electronic SMSI effect from our XPS results due to the similarity of Pd $3d_{5/2}$ binding energy between redox aged Pd/Al to Pd foil. We also did not verify any significant differences in the aged Pd/Al catalyst activity tests, even with different measured Pd dispersion results as the support material had essentially no oxygen mobility. In addition, the reactions selected for this work did not facilitate observations of variable product selectivity, making confirmation of electronic SMSI effects by this route difficult.

4.2. Counteracting SMSI effects with air pulses

The increasing length of air pulses on redox aged Pd/CZO samples showed gradual improvement in Pd surface recovery and catalytic activity indicating a gradual counteracting of SMSI effects relative to the state of the catalyst after continuous redox aging. For the CO DRIFTS spectra on the Pd/CZO samples, the growth rate of carbonaceous species appeared to be directly related to the increasing air pulse length corresponding to the decreasing Ce/Pd ratio in the XPS results in Table 2. The longer air pulses preserved adlineation sites that facilitated rapid growth of carbonaceous species and improved catalytic activity, which were lost with continuous redox aging. After 1 min into a longer air pulse, Pd facets became exposed as CZO decoration retracted similar to other observations in the literature [13,36]. Once exposed, the Pd could now oxidize, migrate, redisperse and shrink according to other microscopy work in the literature [10–12]. An improvement was observed in all three catalyst activity tests for the Pd/CZO redox aged with 2 min of air compared to only 1 min of air. Diminishing returns were observed with 10 min of air compared to 2 min of air, indicating that the Pd-CZO SMSI effects were not completely avoided. Pd/CZO catalyst performance showing complete removal of SMSI effects was presented in our earlier work with lean-only aging environments and post redox aging treatments of air at 700 °C for 2 h where significant support surface area loss and minor Pd sintering were the only deterioration factors [22]. The prior catalyst activity results at 300 °C for the lean-only aged Pd/CZO sample compared to the redox aged Pd/CZO with 10 min of air reveal CO_2 yield performance was within 20%. However, the prior CO DRIFTS work showed the post redox aging treatment of air at 700 °C for 2 h restored CO—Pd peak intensity nearly identical to fresh Pd/CZO, while redox aged Pd/CZO with 10 min of air was not even half of fresh Pd/CZO intensity. Even though the 2 min and 10 min air pulses achieved an improvement to catalytic activity over continuous redox aging, the residual deficiencies in CO DRIFTS and H_2 chemisorption results relative to previous aged Pd/CZO samples without SMSI effects indicate the long time required to reintegrate CZO decorated on the Pd surface back into the bulk support.

Interrupting redox aging with air pulses on Pd/Al samples revealed a large increase in Pd dispersion by H_2 chemisorption in Table 1, which may indicate that periodic oxidation avoids the claimed La$_2$O$_3$ decoration onto Pd as with Ce$_2$O$_3$ [19], but since XRD also showed a Pd dispersion increase, a better explanation that aligns the results of both methods is that Pd redispersion occurred. In addition, no substantial change in surface Pd or La was shown by XPS in Table 3 due to the air pulses that would be required if La was removed from on top of Pd. Whether the Pd-La$_2$O$_3$ SMSI effects were geometric or electronic, the time required

to thoroughly counteract Pd-La$_2$O$_3$ interaction through oxidation was brief. The Pd/Al samples demonstrated rapid Pd dispersion recovery to near the fresh state with just 1/6 min air pulses, compared to the 10 min air pulses required for Pd/CZO. Longer air pulses on aged Pd/Al samples showed small diminishing gains in Pd dispersion by H_2 chemisorption, but did not demonstrate gains in Pd dispersion by XRD, or gains in Pd surface by DRIFTS. These results suggest that SMSI effects between Pd-La$_2$O$_3$ were much faster to uncouple upon oxidation than SMSI decoration effects of CZO support oxide on the Pd surface.

4.3. Limiting Pd sintering with air pulses

The use of air pulses during redox aging was meant to interrupt Pd sintering caused by the aging environment and obtain smaller Pd particles than was measured on the continuous redox aging samples. When samples exhibited decreased Pd size as measured by XRD, it was coincident with the appearance a Pd crystal lattice expansion shown by the leftward shift of XRD pattern Pd peaks in Fig. 2. The reason for this Pd lattice expansion is unclear. While the shift is consistent with Pd hydride formation from the reduction preconditioning step used on all samples, a lattice expansion was observed in just a few samples in Fig. 2. PdO trapped inside a Pd shell can be ruled out as no Pd^{2+} was detected by XPS in any aged sample as shown in Fig. 5 and the center of a 10 nm particle is within the instrument sampling depth. Previously, hollow Pd particles were shown in a STEM image of redox aged Pd/Al samples after a post-aging lean treatment [21], but these particles also did not exhibit a shift in the XRD pattern Pd peak location. Finally, others speculated that high temperature aging of Pd supported on CeO$_2$ or CZO may cause a solid solution to form of Ce in Pd [14,16,61] and Sakamoto et al. showed that about 11% Ce in Pd was sufficient to shift the Pd [111] peak to about 39°2θ [62], which is similar to the trends observed for Pd/CZO in Fig. 2. However, a Pd lattice expansion was also observed on Pd/Al samples that were redox aged with air pulses, and La$_2$O$_3$ is not reducible under our aging conditions.

Electron microscopy revealed that the formation of large Pd particles was more limited using brief interrupting air pulses during redox aging of Pd/Al catalysts, which agreed with XRD estimates of Pd particle size. Interrupting air pulses during redox aging improved Pd dispersion on the Pd/Al catalysts as measured by XRD to 11% versus 6% without air pulses, which was a Pd size reduction down to the fresh Pd size according to volume-averaged microscopy. This Pd redispersion benefit of air pulses as measured by XRD was largely realized through microscopy as a shifting of the Pd size distribution from particles of 20 nm and larger back a few nanometers and creating a new mode at 18 nm. As a result, the numerical average Pd size measured by microscopy of 14.8 nm for continuous versus 14.5 nm for air pulse aging was not statistically different. With the same Pd/Al catalysts that were continuously redox aged under similar conditions in our first study, a post-aging treatment of air at 700 °C for 2 h did show a numerical average Pd size reduction from 16.0 nm to 11.6 nm [21]. The fresh Pd size distribution of our model Pd/Al catalyst was found to have 80% in the size category of 6 nm and less. Perhaps after 10 min of rich aging, the Pd particles sintered to the point where these brief air pulses were not long enough to oxidize all of the Pd particles and enable a thorough Pd redispersion as with the 2 h treatment. A tighter initial Pd particle size distribution with nearly all of the Pd in the 3–4 nm bins may enable more wide-spread Pd redispersion with 10 s air pulses relative to our Pd/Al sample for our aging sequence. In addition, enduring less than 10 min of rich exhaust prior to dry air exposure would cut short sintering induced particle growth, increasing the number of smaller Pd particles that oxidize faster with dry air and redisperse within 10 s, in line with fresh catalyst work by Newton et al. [8].

The technique of repeated transformation of Pd to PdO during redox aging on Pd/CZO required long 10 min air pulses. Cycling rich exhaust with an equal length of air over 16 h was better at keeping Pd small (8 nm by XRD) than applying air at 700 °C for 2 h after 16 h of redox aging as in our first study (24 nm by XRD) [21], and comparable to constant lean aging at 0.1% O_2 as used in our second study (8.6 nm by H_2 chemisorption) [22]. These results appear consistent with work by Kang et al. with Pd-TWC samples aged with a redox-type aging at 600 °C for 16 h while cycling 3% CO for 5 s to form Pd metal then 3% O_2 for 5 s to form PdO [7]. Although the final Pd dispersion was not stated by Kang et al., a lower CO light-off temperature was shown for their redox cycling sample than for aging in constant 3% O_2 [7].

4.4. Catalysts designed for rapid Pd redispersion

The formulation of catalytic converter washcoats are largely based upon maintaining acceptable residual performance after artificially high catalyst aging cycle temperatures needed to compress 150,000 miles of deactivation into a period of hours according to an exponentially time-weighted Arrhenius relationship. The use of air pulses to limit aging effects on Pd-based catalyst performance as shown in this study cannot be successfully incorporated into a higher temperature (850 °C+) aging cycle environment as demonstrated in earlier works [63], but could influence operation under real-world in-use conditions at highway speeds where 700 °C is well within the range of catalyst operating temperatures [21]. However, implementing these engine control actions must be coupled with an automotive catalytic converter washcoat designed both to facilitate rapid Pd redispersion without sacrificing low temperature oxidation activity for automotive emissions. In this work, the aged Pd/Al catalyst was capable of redispersing Pd much faster than the aged Pd/CZO catalyst due to a lack of geometric SMSI effects, but the Pd/Al catalyst was not nearly as active for CO oxidation as the Pd/CZO catalyst. A proper washcoat designed to meet this dual objective would need a combination of thermally stable support material covered with sufficient OSC material to promote Pd for CO oxidation and provide surface oxide sites to enable rapid Pd redispersion in air, yet avoid geometric SMSI effects that counteract both of these desired features. If the engine control actions suggested in this work demonstrate suppressed catalyst deterioration during real-world driving to 150,000 miles with properly formulated catalytic converter washcoats, then aging temperatures on a dynamometer must be lowered to produce catalysts that match performance in the real-world.

5. Conclusions

Continuous redox aging at 700 °C for 16 h on the Pd model catalysts produced different effects depending on the support materials. Continuous redox aged Pd/CZO samples showed no detectable Pd by adsorption of H_2 or CO, and catalyst activity measurement results were significantly degraded towards that of the inert supports suggesting a decoration of Pd by CZO. Continuous redox aged Pd/Al samples also exhibited poor H_2 adsorption on Pd and a discrepancy between XRD and H_2 chemisorption Pd size measurement results, yet after removing surface carbonates then performing room temperature DRIFTS with CO adsorption we observed equally exposed Pd facets for aged and fresh, suggesting a temporary SMSI effect between Pd and La_2O_3 when under a H_2-rich gas environment. Aged Pd/A samples maintained good agreement between XRD and H_2 chemisorption Pd size measurement results indicating no SMSI effects.

We determined the air pulse length required so that any Pd redispersion gains achieved by air treatment during the lean step will not be quickly undone on the following rich step in each 20 min redox aging cycle through 16 h. Air pulses applied to interrupt short redox aging spans enabled Pd redispersion on supports with La_2O_3 and CZO. Air pulses lasting for 1/6 min restored near fresh-like Pd size on the redox aged Pd/Al sample, but did not affect Pd/CZO or Pd/A samples. Air pulses lasting for 2 min were required to begin to detect some surface Pd on the redox aged Pd/CZO samples and observe a significant increase in catalytic activity. Air pulses lasting for 10 min were required to restore near fresh-like Pd size on the redox aged Pd/CZO samples, but did not restore fresh-like Pd facets for CO adsorption or fresh-like catalytic activity. These results suggest that SMSI effects between Pd-La_2O_3 were much faster to uncouple upon oxidation than SMSI decoration effects of CZO support oxide on the Pd surface.

Appendix A. Supplementary data

Supplementary data associated with this article can be found, in the online version, at http://dx.doi.org/10.1016/j.apcatb.2017.07.055.

References

[1] H.S. Gandhi, G.W. Graham, R.W. McCabe, Automotive exhaust catalysis, J. Catal. 216 (2003) 433–442.
[2] J. Kašpar, P. Fornasiero, N. Hickey, Automotive catalytic converters: current status and some perspectives, Catal. Today 77 (2003) 419–449.
[3] R.M. Heck, R.J. Farrauto, Automobile exhaust catalysts, Appl. Catal. A: Gen. 221 (2001) 443–457.
[4] N. Hickey, P. Fornasiero, R. Di Monte, J. Kašpar, J.R. González-Velasco, M.A. Gutiérrez-Ortiz, M.P. González-Marcos, J.M. Gatica, S. Bernal, Reactivation of aged model Pd/$Ce_{0.68}Zr_{0.32}O_2$ three-way catalyst by high temperature oxidising treatment, Chem. Commun. 1 (2004) 196–197.
[5] X. Chen, Y. Cheng, C.Y. Seo, J.W. Schwank, R.W. McCabe, Aging, re-dispersion, and catalytic oxidation characteristics of model Pd/Al_2O_3 automotive three-way catalysts, Appl. Catal. B: Environ. 163 (2015) 499–509.
[6] H. Lieske, J. Völter, Pd redispersion by spreading of PdO in O_2 treated Pd/Al_2O_3, J. Phys. Chem. 89 (1985) 1841–1842.
[7] S.B. Kang, S.J. Han, S.B. Nam, I.S. Nam, B.K. Cho, C.H. Kim, S.H. Oh, Effect of aging atmosphere on thermal sintering of modern commercial TWCs, Top. Catal. 56 (2013) 298–305.
[8] M.A. Newton, C. Belver-Coldeira, A. Martínez-Arias, M. Fernández-García, Oxidationless promotion of rapid palladium redispersion by oxygen during redox CO/(NO + O2) cycling, Angew. Chem. Int. Ed. 46 (2007) 8629–8631.
[9] E.T. Peterson, A.T. DeLaRiva, S. Lin, R.S. Johnson, H. Guo, J.T. Miller, J.H. Kwak, C.H.F. Peden, B. Kiefer, L.F. Allard, F.H. Ribeiro, A.K. Datye, Low-temperature carbon monoxide oxidation catalysed by regenerable atomically dispersed palladium on alumina, Nat. Commun. 5 (2014) 4885.
[10] J.J. Chen, E. Ruckenstein, Role of interfacial phenomena in the behavior of alumina-supported palladium crystallites in oxygen, J. Phys. Chem. 85 (1981) 1606–1612.
[11] N.M. Rodriguez, S.G. Oh, R.A. Dalla-Betta, R.T.K. Baker, In-situ electron microscopy studies of palladium supported on Al_2O_3, SiO_2, and ZrO_2 in oxygen, J. Catal. 157 (1995) 676–686.
[12] E. Ruckenstein, J.J. Chen, Wetting phenomena during alternating heating in O_2 and H_2 of supported metal crystallites, J. Colloid Interface Sci. 86 (1982) 1–11.
[13] A. Badri, C. Binet, J.-C. Lavalley, Metal-support interaction in Pd/CeO_2 catalysis part 2. – Ceria textural effects, J. Chem. Soc. Faraday Trans. 92 (9) (1996) 1603–1608.
[14] L. Kępiński, M. Wolcyrz, J. Okal, Effect of chlorine on microstructure and activity of Pd/CeO_2 catalysts, J. Chem. Soc. Faraday Trans. 91 (1995) 507–515.
[15] H.P. Sun, X.P. Pan, G.W. Graham, H.-W. Jen, R.W. McCabe, S. Thevuthasan, C.H.F. Peden, Partial encapsulation of Pd particles by reduced ceria-zirconia, Appl. Phys. Lett. 87 (2005) 201915.
[16] L. Kępiński, M. Wolcyrz, Microstructure of Pd/CeO_2 catalyst: effect of high temperature reduction in hydrogen, Appl. Catal. A: Gen. 150 (1997) 197–220.
[17] J.S. Rieck, A.T. Bell, Studies of the interactions of H_2 and CO with Pd/SiO_2 promoted with La_2O_3, CeO_2, Pr_6O_{11}, Nd_2O_3, and Sm_2O_3, J. Catal. 99 (1986) 278–292.
[18] J.S. Rieck, A.T. Bell, Studies on the interactions of H_2 and CO with silica- and lanthana-supported palladium, J. Catal. 96 (1985) 88–105.

[19] T.H. Fleisch, R.F. Hicks, A.T. Bell, An XPS study of metal-support interactions on Pd/SiO_2 and Pd/La_2O_3, J. Catal. 87 (1984) 398–413.

[20] R.F. Hicks, Q.J. Yen, A.T. Bell, The influence of metal-support interactions on the catalytic properties of Pd/La_2O_3, Appl. Surf. Sci. 90 (1984) 315–329.

[21] J.A. Lupescu, J.W. Schwank, K.A. Dahlberg, C. Seo, G.B. Fisher, S.L. Peczonczyk, K. Rhodes, M.J. Jagner, L.P. Haack, Pd model catalysts: effect of aging environment and lean redispersion, Appl. Catal. B: Environ. 183 (2016) 343–360.

[22] J.A. Lupescu, J.W. Schwank, G.B. Fisher, X. Chen, S.L. Peczonczyk, A.R. Drews, Pd model catalysts: effect of aging duration and lean redispersion, Appl. Catal. B: Environ. 185 (2016) 189–202.

[23] T.P. Bebee, J.T. Yeates, Spectroscopic detection of (111) facets on supported pd crystallites: site blocking by ethyldyne on Pd/Al_2O_3, Surf. Sci. Lett. 173 (1986) L606–L612.

[24] R.F. Hicks, A.T. Bell, Effects of metal-support interactions on the hydrogenation of CO over Pd/SiO_2 and Pd/La_2O_3, J. Catal. 90 (1984) 205–220.

[25] D. Briggs, M.P. Seah, Practical Surface Sci. Analysis by Auger and X-ray Photoelectron Spectroscopy, John Wiley & Sons, New York, 1984.

[26] S. Tanuma, C.J. Powell, D.R. Penn, Calculations of electron inelastic mean free paths (IMFPS). IV. Evaluation of calculated IMFPs and of the predictive IMFP formula TPP-2 for electron energies between 50 and 2000 eV, Surf. Interface Anal. 21 (1993) 165.

[27] A.L. Patterson, The Scherrer formula for X-Ray particle size determination, Phys. Rev. 56 (1939) 978–982.

[28] C.R. Adams, H.A. Benesi, R.M. Curtis, R.G. Meisenheimer, Particle size determination of supported catalytic metals: platinum on silica gel, J. Catal. 1 (1962) 336–344.

[29] J.K. Plischke, M.A. Vannice, Effect of pretreatment on the adsorption properties of silver crystallites, Appl. Catal. 42 (1988) 255–283.

[30] R.T.K. Baker, E.B. Prestridge, G.B. McVicker, The interaction of palladium with alumina and titanium oxide supports, J. Catal. 89 (1984) 422–432.

[31] F.M. Dautzenberg, H.B.M. Wolters, State of dispersion of platinum in alumina-supported catalysts, J. Catal. 51 (1978) 26–39.

[32] A. Baylet, S. Royer, P. Marécot, J. Tatibouët, D. Duprez, Effect of Pd precursor salt on the activity and stability of Pd-doped hexaaluminate catalysts for the CH_4 catalytic combustion, Appl. Catal. B: Environ. 81 (2008) 88–96.

[33] J.E. Benson, H.S. Hwang, M. Boudart, Hydrogen-oxygen titration method for the measurement of supported palladium surface areas, J. Catal. 30 (1973) 146–153.

[34] V. Ragaini, R. Giannantonio, P. Magni, L. Lucarelli, G. Leofanti, Dispersion measurement by the single introduction method coupled with the back-sorption procedure: a chemisorption and TPD study of the different chemisorbed hydrogen species II. Pd on alumina, J. Catal. 146 (1994) 116–125.

[35] T. Takeguchi, S. Manabe, R. Kikuchi, K. Eguchi, T. Kanazawa, S. Matsumoto, W. Ueda, Determination of dispersion of precious metals on CeO_2-containing supports, Appl. Catal. A: Gen. 293 (2005) 91–96.

[36] M. Alexandrou, R.M. Nix, The growth, structure and stability of ceria overlayers on Pd(111), Surf. Sci. 321 (1994) 47–57.

[37] A.J. Hayter, Probability and Statistics for Engineers and Scientists, PWS Publishing Co., Boston, MA, 1996.

[38] J.Z. Shyu, K. Otto, W.L.H. Watkins, G.W. Graham, R.K. Belitz, H.S. Gandhi, Characterization of Pd γ-alumina catalysts containing ceria, J. Catal. 114 (1988) 23–33.

[39] M. Zhao, X. Li, L. Zhang, C. Zhang, M. Gong, Y. Chen, Catalytic decomposition of methanol to carbon monoxide and hydrogen over palladium supported on $Ce_{0.65}Zr_{0.30}La_{0.05}O_2$ and La–Al_2O_3, Catal. Today 175 (2011) 430–434.

[40] L. Yang, X. Yang, S. Lin, R. Zhou, Insights into the role of a structural promoter (Ba) in three-way catalyst Pd/CeO_2–ZrO_2 using in situ DRIFTS, Catal. Sci. Technol. 5 (2015) 2688–2695.

[41] K. Tanikawa, C. Egawa, Effect of barium addition on CO oxidation activity of palladium catalysts, Appl. Catal. A: Gen. 403 (2011) 12–17.

[42] M.Y. Smirnov, G.W. Graham, Pd oxidation under UHV in a model Pd/ceria-zirconia catalyst, Catal. Lett. 72 (2001) 39–44.

[43] C. Yang, J. Ren, Y. Sun, Role of La_2O_3 in Pd-supported catalysts for methanol decomposition, Catal. Lett. 84 (2002) 123–129.

[44] A. Holmgren, B. Anderson, D. Duprez, Interactions of CO with Pt/ceria catalysts, Appl. Catal. B: Environ. 22 (1999) 215–230.

[45] G.N. Vayssilov, M. Mihaylov, P. St. Petkov, K.I. Hadjiivanov, K.M. Neyman, Reassignment of the vibrational spectra of carbonates, formates, and related surface species on ceria: a combined density functional and infrared spectroscopy investigation, J. Phys. Chem. C 115 (2011) 23435–23454.

[46] N.B. Colthup, Spectra-structure correlations in the infra-red region, J. Opt. Soc. Am. 40 (1950) 397–400.

[47] F.M. Hoffmann, Infrared reflection-absorption spectroscopy of adsorbed molecules, Surf. Sci. Rep. 3 (1983) 107–192.

[48] J. Szanyi, W.K. Kuhn, D.W. Goodman, CO adsorption on Pd(111) and Pd(100): low and high pressure correlations, J. Vac. Sci. Technol. A 11 (1993) 1969–1974.

[49] S. Bertarione, D. Scarano, A. Zecchina, V. Johánek, J. Hoffmann, S. Schauermann, M.M. Frank, J. Libuda, G. Rupprechter, H.-J. Freund, Surface reactivity of Pd nanoparticles supported on polycrystalline substrates as compared to thin film model catalysts: infrared study of CO adsorption, J. Phys. Chem. B 108 (2004) 3603–3613.

[50] T. Lear, R. Marshell, J.A. Lopez-Sanchez, S.D. Jackson, T.M. Klapötke, M. Bäumer, G. Rupprechter, H.-J. Freund, D. Lennon, The application of infrared spectroscopy to probe the surface morphology of alumina supported palladium catalysts, J. Chem. Phys. 123 (2005) 174706.

[51] G. Graham, H. Jen, W. Chun, R. McCabe, Encapsulation of Pd particles by ceria-zirconia mixed oxides, Catal. Lett. 44 (1997) 185–187.

[52] J.M. Gatica, R.T. Baker, P. Fornasiero, S. Bernal, J. Kašpar, Characterization of the metal phase in $NM/Ce_{0.68}Zr_{0.32}O_2$ (NM: Pt and Pd) catalysts by hydrogen chemisorption and HRTEM microscopy: a comparative study, J. Phys. Chem. B 105 (2001) 1191–1199.

[53] X.L. Seoane, N.S. Figoli, P.C. L'Argentiere, J.A. González, A. Arcoya, Palladium-lanthanum interaction phenomena in Pd-$LaCl_3$/SiO_2 and Pd-La_2O_3/SiO_2 catalysts, Catal. Lett. 47 (1997) 213–220.

[54] W.H. Cassinelli, L.S.F. Feio, J.C.S. Araújo, C.E. Hori, F.B. Noronha, C.M.P. Marques, J.M.C. Bueno, Effect of CeO_2 and La_2O_3 on the activity of CeO_2-La_2O_3/Al_2O_3-supported Pd catalysts for steam reforming of methane, Catal. Lett. 120 (2008) 86–94.

[55] M. Shelef, L.P. Haack, R.E. Soltis, J.E. deVries, E.M. Logothetis, An XPS study of interactions in thin films containing a noble metal with valence-lnvariant and reducible oxides, J. Catal. 137 (1992) 114–126.

[56] J.R. Gaudet, A. de la Riva, E.J. Peterson, T. Bolin, A.K. Datye, Improved low-temperature CO oxidation performance of Pd supported on La-stabilized alumina, ACS Catal. 3 (2013) 846–855.

[57] I.Y. Ahn, W.J. Kim, S.H. Moon, Performance of La_2O_3- or Nb_2O_5- added Pd/SiO_2 catalysts in acetylene hydrogenation, Appl. Catal. A: Gen. 308 (2006) 75–81.

[58] E. Kim, E.W. Shin, C.W. Bark, I. Chang, W.J. Yoon, W.J. Kim, Pd catalyst promoted by two metal oxides with different reducibilities: properties and performance in the selective hydrogenation of acetylene, Appl. Catal. A: Gen. 471 (2014) 80–83.

[59] E.H. Voogt, A.J.M. Mens, O.L.J. Gijzeman, J.W. Geus, Adsorption of oxygen and surface oxide formation on Pd(111) and Pd foil studied with ellipsometry, LEED, AES and XPS, Surf. Sci. 373 (1997) 210–220.

[60] R. Price, T. Eralp-Erden, E. Crumlin, S. Rani, S. Garcia, R. Smith, L. Deacon, C. Euaruksakul, G. Held, The partial oxidation of methane over Pd/Al_2O_3 catalyst nanoparticles studied in-situ by near ambient-pressure X-ray photoelectron spectroscopy, Top. Catal. 59 (2016) 516–525.

[61] S. Bernal, J.J. Calvino, M.A. Cauqui, J.M. Gatica, C. Larese, J.A. Pérez Omil, J.M. Pintado, Some recent results on metal/support interaction effects in NM/CeO_2 (NM: noble metal) catalysts, Catal. Today 50 (1999) 175–206.

[62] Y. Sakamoto, K. Takao, M. Ohmaki, The phase transitions in the palladium-rich Pd-Ce alloy system, J. Less-Common Met. 162 (1990) 343–359.

[63] R.M. Heck, J.K. Hochmuth, J.C. Dettling, Effect of oxygen concentration on aging of TWC catalysts, SAE Tech. Pap. 920098 (1992), http://dx.doi.org/10.4271/920098.